Evolution of anisotropy in direct numerical simulations of MHD turbulence in a strong magnetic field on elongated periodic domains

X. M. Zhai and P. K. Yeung

Phys. Rev. Fluids **3**, 084602 — Published 7 August 2018

DOI: 10.1103/PhysRevFluids.3.084602

The evolution of anisotropy in direct numerical simulations of MHD turbulence in a strong magnetic field on elongated periodic domains

X.M. Zhai

School of Aerospace Engineering, Georgia Institute of Technology, Atlanta, GA 30332, USA

P.K. Yeung

Schools of Aerospace Engineering and Mechanical Engineering,
Georgia Institute of Technology, Atlanta, GA 30332, USA *

(Dated: July 16, 2018)

Abstract

The response of initially isotropic turbulence to a strong magnetic field in the low magnetic Reynolds number regime has been studied using direct numerical simulations on elongated solution domains that are necessary for reliable results at long evolution times. Most results are obtained using a 16384×2048^2 periodic domain of aspect ratio 8, without numerical forcing, after a pre-simulation that creates the desired initial conditions before the magnetic field is applied. At early times, velocity fluctuations parallel to the magnetic field becomes dominant as a result of Joule dissipation being weaker in this direction. However, this anisotropy is reversed after several large-eddy time scales. Statistics of the velocity gradients indicate a strong trend towards local axisymmetry and quasi-two-dimensionality, with reduced intermittency. Scale-dependent anisotropy is studied in spectral space in terms of a wavenumber (k_1) along the magnetic field and a radial wavenumber (k_r) in the orthogonal plane. Axisymmetric spectra show that the Joule dissipation plays a dominant role in causing kinetic energy to be concentrated in a narrow spectral region at very low values of k_1, which would not be captured if the domain were cubic. Simulations spanning over two orders of magnitude variation in the magnetic interaction parameter (N) show that Reynolds stress anisotropy scales with the Joule time only for a short initial period. At large N, accelerated development of anisotropy leads to an even greater need for elongated domains which have not been employed frequently in the literature. Overall the results in this work provide both a confirmation of trends seen in simulations on cubic domains at earlier times and new observations at later times where the benefits of an elongated domain are clearly evident. A clear parameterization of Reynolds number effects still awaits larger simulations at inevitably higher cost.

I. INTRODUCTION

The study of magnetohydrodynamic (MHD) turbulence of an electrically conducting fluid subjected to a magnetic field has numerous applications ranging from metallurgical processing to astrophysical phenomena[1,2]. The motion of the fluid produces an electric field, and hence a current, which modifies the character of the flow field dramatically through the Lorentz force that points in a direction orthogonal to both the electric current and magnetic field vectors. In general, the resulting flow phenomena depend strongly on the the magnetic Reynolds number (R_m), which is a measure of the strength of advective transport to that of diffusion of the magnetic field. However, in most terrestrial applications, including convection in the Earth's core, and nuclear reactor design, R_m is much smaller than unity — in which case the velocity field has only a minimal effect on the magnetic field. The main interest is then in how the velocity field is (in a one-way coupling) modified by the magnetic field. For MHD turbulence in this low magnetic Reynolds number regime the strength of MHD effects is expected to be a function of how the time scale of the magnetic field compares with the time scale(s) of the turbulence itself.

Since liquid metals are opaque and corrosive, experiments in MHD turbulence are much more difficult than those involving ordinary fluids. As a result, direct numerical simulations, if formulated properly and executed efficiently, have particular appeal for understanding the fundamentals in this subject[3]. A number of authors have simulated MHD turbulence in a simplified geometry, namely a three-dimensional (3D) periodic domain, with (e.g. Refs. 4–7) or without (e.g. Refs. 8–10) numerical forcing that supplies energy to the large scales. These studies have shown, for instance, that length scales under MHD can grow rapidly, and that Joule dissipation arising from the Lorentz force causes the energetics of the flow to differ substantially from classical isotropic turbulence. However, although the use of (different types of) forcing as a means of achieving stationarity at high Reynolds number in hydrodynamic turbulence[11,12] is well accepted, for MHD turbulence this may interfere with the physical effects of the Lorentz force, which acts at all scales. On the other hand, if the turbulence is allowed to decay without energy input the Reynolds number in numerical simulations often becomes quite low, especially if the range of scales is limited by a desire to minimize effects of finite domain size[9]. At the same time, although (for this reason) computational requirements for MHD turbulence are greater than those for hydrodynamic turbulence, simulations of MHD turbulence have generally not yet reached the grid resolutions deployed for the latter (such as in Ref. 13 and higher). Furthermore, in view of preferential growth of large-eddy length scales along the direction of the imposed magnetic field, cubic solution domains widely employed in the literature are physically not optimal.

The basic premise of our work in this paper is to improve understanding of MHD turbulence by conducting simulations of higher resolution than achieved before in this subject, using elongated solution domains of large aspect ratio, with initial flow conditions that are representative of natural, unforced isotropic turbulence. Our first focus is on the anisotropy that develops at various scales as a result of the Lorentz force, through a dissipative mechanism which (unlike viscous dissipation) is inherently anisotropic. Previous works in the literature[14,15] have in fact suggested a trend towards quasi two-dimensionality (hereafter Q2D for short) if the magnetic field is sufficiently strong. To analyze the anisotropy we consider the single-point Reynolds stress tensor, the statistics of velocity gradients under constraints due to axisymmetry[16], as well as evolution of spectral quantities in Fourier space[17]. Anisotropy also implies that both magnitude and orientation in wavenumber space are important. We mainly use the tools of one-dimensional and axisymmetric spectra[18] which can provide information complementary to other descriptions such as a decomposition into toroidal and poloidal contributions[10], ring-to-ring energy transfer[17,19], as well as wavelet analyses[20].

Our second focus is to quantify the effects of the strength of the imposed magnetic field, through the magnetic interaction parameter (N), defined as the ratio of a large-eddy time scale of an initial turbulence state to the time scale (called Joule time) of the magnetic field. Although other authors have reported results for values of N much larger than unity before, we show that simulation results at large N can be unreliable (except perhaps at early times) unless domain size requirements are addressed rigorously. For example, use of elongated domains allows us to compare our results with an asymptotic prediction by Moffatt[21] for anisotropy development in the limit of infinitely large N. A more general question is whether changes in turbulence statistics scale with the Joule time of the magnetic field. For the study of effects of larger N the use of elongated domains to minimize the confinement effects on the turbulence structure due to insufficient domain size is even more important. It may be noted that such confinement effects may be avoided entirely in an alternative approach based on spectral closures[10,22], while other phenomena such as Hartmann layers are present in flows with actual solid boundaries[23–25]. However we shall not consider those effects in this work.

In this paper we present results from a number of simulations. In each case, a pre-simulation of decaying isotropic turbulence is first performed to provide physically realistic initial conditions prior to the activation of the magnetic field. The domain aspect ratio is varied from 1 to 64, and the magnetic interaction parameter is varied from 1 to 256. The highest grid resolution employed is 16384×2048^2, for simulations where the pre-MHD Taylor-scale Reynolds number is 98. At early times velocity fluctuations parallel to the imposed magnetic field are larger than those in the orthogonal directions, but the inequality is reversed at later times. In the literature this anisotropy reversal has been interpreted[10] as the result of polarization in spectral space. However we attempt to provide a more detailed analysis, over a range of values of N as stated above. In particular, we examine the direct and indirect effects of the Joule dissipation in the evolution of different terms in the Reynolds stress budget, and the development of Q2D behavior as well as departures from local isotropy at the small scales. We also present results on one-dimensional and axisymmetric spectra[18] of the turbulence kinetic energy as well as specific terms in the spectral energy budget, including nonlinear spectral transfer and contributions from pressure-strain correlations.

The remaining sections of this paper are organized as follows. In Sec. II we give a brief summary of our technical approach, including equations and numerical methods. In Sec. III we discuss the use of pre-simulations on domains of appropriate size and aspect ratio to obtain initial conditions for our MHD simulations. A basic assessment of the effects of aspect ratio on the development of basic quantities such as the turbulence kinetic energy and viscous and Joule dissipation rates is also given. The bulk of our numerical results is presented in Sec. IV, mainly using a 16384×2048^2 simulation with $N = 1$. Separate subsections are devoted to studies of Reynolds stress anisotropy, statistics of the small scales, and spectral characteristics as a function of wavenumbers parallel and perpendicular to the imposed magnetic field. In Sec. V we address the effects of larger values of N, using two separate series of simulations at resolutions 4096×512^2 and 16384×2048^2. Finally in Sec. VI we summarize the conclusions of this work and briefly point to additional investigations which will be reported separately in the future.

II. BACKGROUND AND NUMERICAL PROCEDURES

Davidson[26] gives a detailed derivation of MHD equations. If $\mathbf{B}$ is the magnetic field then the Lorentz force is $(\mathbf{J} \times \mathbf{B})$ per unit volume, where $\mathbf{J} = \nabla \times \mathbf{B}/\mu$ is the current density, and μ is the permeability of free space. By decomposing the Lorentz force into irrotational and solenoidal contributions we can write the momentum equation for velocity fluctuations $\mathbf{u}$ (with no mean velocity) in the form

$$\frac{D\mathbf{u}}{Dt} = -\frac{1}{\rho}\nabla(p + \frac{B^2}{2\mu}) + \nu\nabla^2\mathbf{u} + \frac{1}{\rho\mu}\mathbf{B}\cdot\nabla\mathbf{B} \tag{1}$$

where D/Dt denotes the material derivative operator, ρ is the fluid density, p is the (hydrodynamic) pressure, $B \equiv |\mathbf{B}|$, μ is the permeability of free space, and ν is the kinematic viscosity. We let $\mathbf{B} = \mathbf{B}_0 + \mathbf{b}$, where $\mathbf{B}_0$ is steady and uniform, and $\mathbf{b}$ is the fluctuating magnetic field. The magnetic Reynolds number R_m may be defined as $\mathcal{UL}/\zeta$ where $\mathcal{U}$ and $\mathcal{L}$ are typical velocity and length scales of the flow, and $\zeta = 1/(\mu\sigma)$ is the magnetic diffusivity (and σ is the electrical conductivity). If $R_m \ll 1$ the magnetic field fluctuation is weak (i.e. $|\mathbf{b}| \ll |\mathbf{B}_0|$), and the resulting quasi-static approximation gives $\mathbf{b} = \nabla^{-2}[-(1/\zeta)\mathbf{B}_0 \cdot \nabla\mathbf{u}]$. This relation can be used to obtain the Lorentz force. The momentum equation then becomes

$$\partial\mathbf{u}/\partial t + \mathbf{u}\cdot\nabla\mathbf{u} = -(1/\rho)\nabla(p + B^2/2\mu) - (\sigma/\rho)[(\mathbf{B}_0\cdot\nabla)^2(\nabla^{-2}\mathbf{u})] \; + \nu\nabla^2\mathbf{u} \; , \tag{2}$$

which can be readily transformed to Fourier space. By letting $\mathbf{B}_0$ be aligned with one of the coordinate axes (say, x, or equivalently, x_1) and projecting onto a plane perpendicular to the wave-vector $\mathbf{k}$ to enforce incompressibility, we obtain the equation

$$\partial\hat{\mathbf{u}}(\mathbf{k})/\partial t = -[\widehat{\mathbf{u}\cdot\nabla\mathbf{u}}]_{\perp\mathbf{k}} - (\sigma/\rho)B_0^2(k_x/k)^2\hat{\mathbf{u}} - \nu k^2\hat{\mathbf{u}} \tag{3}$$

where k is the magnitude of $\mathbf{k}$, and overhats denote Fourier coefficients, and the subscript $\perp\mathbf{k}$ denotes the projection operator. The second term on the right of Eq. (3) is the origin of the Joule dissipation effect, which provides magnetic damping in various applications. Since (unlike viscous dissipation) Joule dissipation depends on orientation in wavenumber space but not scale size, it tends to induce anisotropy, at all scales. Numerically, since the Lorentz force in Eq. (3) is (like the viscous term) linear in the velocity, in Fourier pseudo-spectral algorithms it can be treated exactly via an integration factor for integration in time, at no significant extra cost regardless of the magnetic field. We use a second-order Runge Kutta scheme, in which aliasing errors are controlled by truncation and phase shifting techniques[27]. The simulations have been performed with a massively parallel DNS code, that uses a two-dimensional domain decomposition to facilitate large CPU core counts, and can also allow shared memory multi-threading among multiple cores per node. Results reported in this paper were almost exclusively obtained using the computational resources at the Texas Advanced Computing Center (TACC). The computational cost per time step for the largest simulation at 16384×2048^2 resolution is similar to that for a 4096^3 grid which has the same number of grid points.

In this work we study anisotropy development using several scale-dependent quantities in physical and spectral spaces, beginning with the Reynolds stress tensor, which evolves by

$$d\langle u_i u_j\rangle/dt = (2/\rho)\langle p s_{ij}\rangle - \langle J_{ij}\rangle - \langle\epsilon_{ij}\rangle \tag{4}$$

where $s_{ij} \equiv (\partial u_i/\partial x_j + \partial u_j/\partial x_i)/2$ is the strain rate tensor, and angled brackets represent averaging in space, and terms on the right are the pressure-strain correlation, Joule and viscous dissipation tensors respectively. The last two terms can be related to the velocity spectrum tensor $\Phi_{ij}(\mathbf{k})$ (whose integral is the Reynolds stress) by

$$\langle J_{ij} \rangle = 2(\sigma B_0^2/\rho) \iiint (k_x/k)^2 \Phi_{ij}(\mathbf{k})\ d\mathbf{k} \ \ ; \ \langle \epsilon_{ij} \rangle = 2\nu \iiint k^2 \Phi_{ij}(\mathbf{k})\ d\mathbf{k} \ . \tag{5}$$

Taking half of the traces of these relations gives the dissipation rates, via

$$\langle J \rangle = 2(\sigma B_0^2/\rho) \iiint (k_x/k)^2 E(\mathbf{k})\ d\mathbf{k} \ \ ; \ \langle \epsilon \rangle = 2\nu \iiint k^2 E(\mathbf{k})\ d\mathbf{k} \ , \tag{6}$$

where $E(\mathbf{k}) = \frac{1}{2}\Phi_{ii}(\mathbf{k})$ is the 3D energy spectrum.

Since MHD turbulence has very different length scales in different directions, representation of anisotropy as a function of wavenumber magnitude k in wavenumber space would not be satisfactory. Instead, we note that the turbulence studied is axisymmetric, with rotational symmetry[28] around the direction of the imposed magnetic field. As in Ref. 18 we may thus represent the spectral content of the turbulence as a function of one-dimensional wavenumber k_1 (same as k_x, along the direction of the magnetic field) and a "radial" wavenumber $k_r = \sqrt{k_2^2 + k_3^2}$ in the transverse plane. In this coordinate system $k_r = k \sin\phi$ where $0 \le \phi \le \pi$ is the co-latitude with respect to the k_1 axis, and $0 \le \theta \le 2\pi$ is the polar angle within the $k_2 - k_3$ plane. The axisymmetric spectrum tensor can be formed by integrating the velocity spectrum tensor over all values of θ, i.e.

$$A_{ij}(k_1, k_r) = \int_0^{2\pi} \Phi_{ij}(\mathbf{k}) k_r \ d\theta \ . \tag{7}$$

The velocity spectrum in one dimension can also be recovered by

$$\Phi_{ij}(k_1) = 2 \int_0^{\infty} A_{ij}(k_1, k_r)\ dk_r \tag{8}$$

where the factor of 2 accounts for contributions from both positive and negative k_1. Half of the trace of $A_{ij}(k_1, k_r)$ gives the axisymmetric energy spectrum, $E_A(k_1, k_r)$. If the turbulence is isotropic a contour plot of $E_A(k_1, k_r)/\sin\phi$[29] would show a pattern of concentric circles. Any deviation from such circular contours (except caused by a limited number of Fourier modes at low k_1 or low k_r) is then an indicator of anisotropy. A radial spectrum in k_r can also be defined, such that

$$\Phi'_{ij}(k_r) = \int_0^{\infty} A_{ij}(k_1, k_r)\ dk_1 \ . \tag{9}$$

In practice, the upper limits of the integrals in Eqs. (8) and (9) are replaced by the highest wavenumbers in k_1 or k_r represented in the code after treatment for aliasing errors[27].

III. INITIAL CONDITIONS AND DOMAIN ASPECT RATIO

To study the response of isotropic turbulence to the magnetic field it is important to begin with a physically realistic isotropic state — that can be represented well in an anisotropic

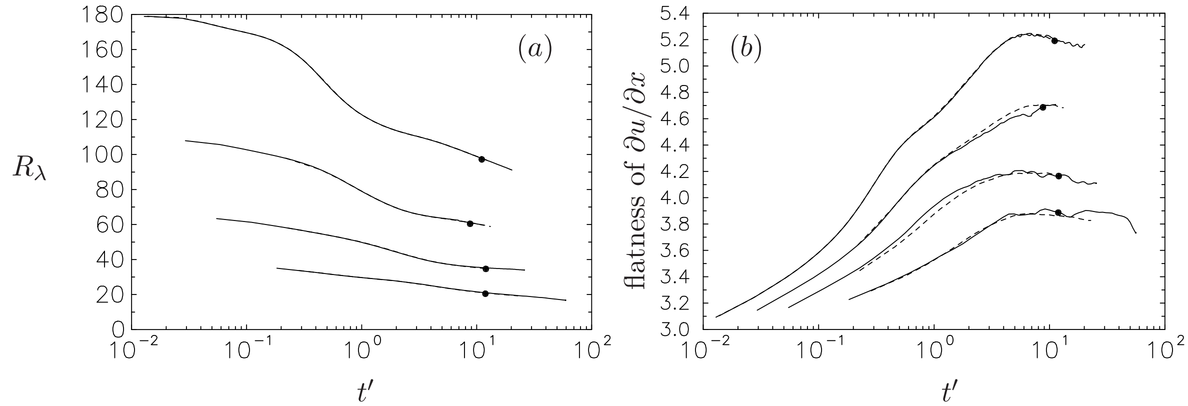

FIG. 1. (a) Taylor-scale Reynolds number and (b) flatness factor of longitudinal velocity gradients in pre-simulations where $n_y = n_z = 256$, 512, 1024, 2048 (from bottom to top). With $n_x = \Lambda n_y$, results for $\Lambda = 1$ and $\Lambda = 8$ are indicated by solid lines and dashed lines respectively. The time axis (t') is normalized by initial values of K and $\langle\epsilon\rangle$ in the pre-simulation. The meanings of the circles on each curve are addressed in the text.

domain of non-unity aspect ratio, with minimal numerical distortion. A pre-simulation where isotropic turbulence is allowed to evolve naturally is typically required. Here we present a summary of these pre-simulations and an assessment of how high an aspect ratio is required for reliable results.

We consider solution domains of lengths $\mathcal{L}_{0x}$, $\mathcal{L}_{0y}$ $\mathcal{L}_{0z}$ in x, y, z directions with n_x, n_y and n_z grid points respectively. The magnetic field is applied in the x direction, on elongated domains of aspect ratio $\Lambda = \mathcal{L}_{0x}/\mathcal{L}_{0y} > 1$, while $\mathcal{L}_{0y} = \mathcal{L}_{0z}$. In each direction the number of grid points is proportional to the length of the solution domain, so that the grid spacings Δx, Δy and Δz are all equal. This ensures small-scale motions are equally well resolved in every coordinate direction, with the same highest wavenumbers in each. We set $\mathcal{L}_{0y} = \mathcal{L}_{0z} = 2\pi$ units, with Λ increased from unity in powers of 2, as desired.

To achieve the objective of minimum numerical distortion, the large eddies prior to activation of the magnetic field must be very small compared with the dimensions of the solution domain. The purpose of the pre-simulations is to allow the turbulence to develop naturally towards a well-developed state, with initial parameters chosen to minimize numerical artifacts. We initialize the flow as a Gaussian velocity field with an energy spectrum function (which is the integral of $E(\mathbf{k})$ over a spherical shell of radius k in wavenumber space) of the form[30]

$$E(k) = C_K \langle\epsilon\rangle^{2/3}\; k^{-5/3} f_L(kL) f_\eta(k\eta) \tag{10}$$

where $C_K \approx 1.62$ (Ref. 31) is the Kolmogorov constant for $E(k)$, L and η are initial (longitudinal) integral and Kolmogorov scales respectively, and $f_L(\cdot)$ and $f_\eta(\cdot)$ are semi-empirical fitting functions. As the turbulence decays all the length scales are expected to grow. It is important to choose L here to be very small compared to the domain size in all directions, so that even at the end of the pre-simulation ample room remains for the large scales to grow during the subsequent MHD simulation. The pre-simulation can be considered complete when the kinetic energy shows a power-law decay while the Reynolds number drops slowly, and when clear non-Gaussianity in the velocity gradients has developed.

Figure 1 shows the evolution of Taylor-scale Reynolds number (R_λ) and flatness factor of longitudinal velocity gradients in several pre-simulations that began at different Reynolds numbers, with L taken to be 1/48 of the shortest sides of the domain. The gradient flatness increases from 3.0, towards a maximum and then decreases as a result of a slowly decreasing Reynolds number. Solid and dashed lines for pre-simulations on cubic and elongated domains with $\Lambda = 8$ (and $n_x = \Lambda n_y$) are in close agreement, thus showing that a proper isotropic state has been attained on an anisotropic solution domain. Velocity fields at time instants marked by solid circles are used as initial conditions for our MHD simulations.

Grid points	2048×256^2	4096×512^2	8192×1024^2	16384×2048^2
ν	0.0028	0.0011	0.000437	0.0001732
n_R	3	2	3	2
$(R_\lambda)_b$	36	62	105	173
$(R_\lambda)_0$	21	35	61	98
u'	0.393	0.350	0.428	0.383
v'	0.394	0.351	0.430	0.385
w'	0.394	0.350	0.430	0.386
L_1/L_2	1.999	1.941	2.026	1.981
$\langle(\nabla_\parallel \mathbf{u})^2\rangle/\langle(\nabla_\perp \mathbf{u})^2\rangle$	0.5001	0.4998	0.5000	0.4999
μ_3 of $\nabla_\parallel \mathbf{u}$	-0.497	-0.508	-0.519	-0.529
μ_4 of $\nabla_\parallel \mathbf{u}$	3.863	4.174	4.701	5.212
$\mathcal{L}_{0\parallel}/L_1$	130	134	166	163
$\mathcal{L}_{0\perp}/L_1$	16.3	16.8	20.8	20.4
$\Delta x/\eta$	1.479	1.302	1.519	1.356

TABLE I. Parameters of pre-simulations for domains of aspect ratio 8 (with shortest side fixed at 2π): viscosity, Taylor-scale Reynolds number $(R_\lambda)_b$ before the pre-simulation begins, followed by various parameters (as discussed in the text) at the end of the pre-simulation.

Table I shows parameters for pre-simulations on domains of aspect ratio $\Lambda = 8$. As in simulations of forced isotropic turbulence[32], higher Reynolds numbers are obtained on finer grids by reducing the viscosity (ν). Ensemble averaging is taken over modest number (n_R) of realizations initialized with different random number seeds. It is clear that, despite the solution domain being highly anisotropic, the component r.m.s velocities, the ratio between longitudinal (L_1) and transverse (L_2) integral length scales, and the ratio between mean-squared longitudinal ($\nabla_\parallel \mathbf{u}$) and transverse ($\nabla_\perp \mathbf{u}$) velocity gradient fluctuations all agree very well with results in incompressible isotropic turbulence. The skewness (μ_3) and flatness (μ_4) factors of $\nabla_\parallel \mathbf{u}$ are also close to values at comparable Reynolds numbers in simulations of forced isotropic turbulence[33]. The ratios of domain sizes to the integral length scales at the end of the pre-simulation are sufficiently large for the large scales to develop naturally under a magnetic field in the x direction. Resolution of the Kolmogorov scale is also adequate, and is expected to improve further as the turbulence continues to decay.

For a given pre-MHD turbulence state subjected to a magnetic field of strength B_0 in a fluid of density ρ and conductivity σ, MHD effects can be characterized by the magnetic interaction parameter (N) as the ratio of a large-eddy time scale to the Joule time $\tau_J \equiv \rho/(\sigma B_0^2)$. We use the eddy turnover time $T_E = L_{11}/u'$ where L_{11} is a longitudinal length scale and u' is the r.m.s. velocity as the large-eddy time scale. Other definitions (such as $K/\langle\epsilon\rangle$) have been used by others as well but that will not change our results significantly. We note that some theoretical results are known for N of order unity[5,9] as well as $N \to \infty$[21].

Grid	Λ	n_R	$(R_\lambda)_0$	N
256^3	1	3	21	0.5,1,2
512×256^2	2	3	21	1
1024×256^2	4	3	21	1
2048×256^2	8	3	21	1
4096×256^2	16	3	21	1
8192×256^2	32	4	21	1
16384×256^2	64	3	21	1
4096×512^2	8	2	34	0.5,1,2,4,8,16,32,64,128,256
2048×256^2	8	3	21	1
4096×512^2	8	2	34	0.5,1,2,4,8,16,32,64,128,256
8192×1024^2	8	3	59	0.1,0.5,1,2,5,10
16384×2048^2	8	2	98	1,2,4,8
2048^3	1	1	98	1,8

TABLE II. Table of parameters for production MHD simulations studied in this paper.

Stronger magnetic fields with shorter time scales lead to faster growth of the large-eddy length scales and hence turbulence statistics becoming contaminated by finite domain size effects earlier. We generally use data only at times before at least one integral length scale in the x direction exceeds 1/4 of $\mathcal{L}_{0x}$. For the same physical parameters a domain with larger Λ allows reliable results to be obtained for a longer period of time. Table II gives a list of the key simulations in this work, grouped into three categories used to study dependence on domain aspect ratio, magnetic interaction parameter and pre-MHD Reynolds number respectively. In our simulations, as the integral length scales grow while the turbulence decays, the value of N if based on instantaneous values of T_E can increase by 2 orders of magnitude of more (even more so than in simulations with forcing[4,17]). For convenience, and since the magnetic field itself is fixed, we use values of N based on the value of T_E just before the magnetic field is applied.

Figure 2 gives, in three frames, a basic characterization of effects of MHD in our simulations. When the magnetic field is turned on (at time t_0), the kinetic energy decreases more quickly (as a direct result of the Joule dissipation) than in freely decaying isotropic turbulence but reverts later to power-law behavior. The integral length scales grow rapidly: in particular, L_{11} is seen to grow to 4.6 and beyond (which is 6 times of L_{22}), which would not have been captured if the solution domain were a cube of size $(2\pi)^3$. Anisotropy reflected by nonzero values of the Reynolds stress anisotropy tensor $b_{ij} = \langle u_i u_j \rangle/(2K) - (1/3)\delta_{ij}$, develops quickly when the magnetic field is turned on. At short times $t - t_0$ $b_{11} > 0$ while $b_{22} \approx b_{33} < 0$, but this anisotropy is reversed at later times.

To help quantify the sensitivity of numerical results to the domain aspect ratio, in Fig. 3 we compare the evolution of (a) longitudinal integral length scale (L_{11}), (b) Joule dissipation and (c) viscous dissipation for simulations at Λ from 1 to 64 (in powers of 2), with $(R_\lambda)_0$ and N held fixed (at 21 and 1 respectively). In this and all subsequent figures we define normalized time t^* as $(t - t_0)/(T_E)_0$ where the subscript 0 refers to pre-MHD conditions. Since L_{11} is an integral of the two-point correlation for spatial separation r_x from 0 to $\frac{1}{2}\mathcal{L}_{0x}$ its maximum possible value is $\frac{1}{2}\mathcal{L}_{0x}$ which is marked by short horizontal bars in frame (a). At early times, all curves agree closely with each other. (Conversely, the benefits of larger Λ

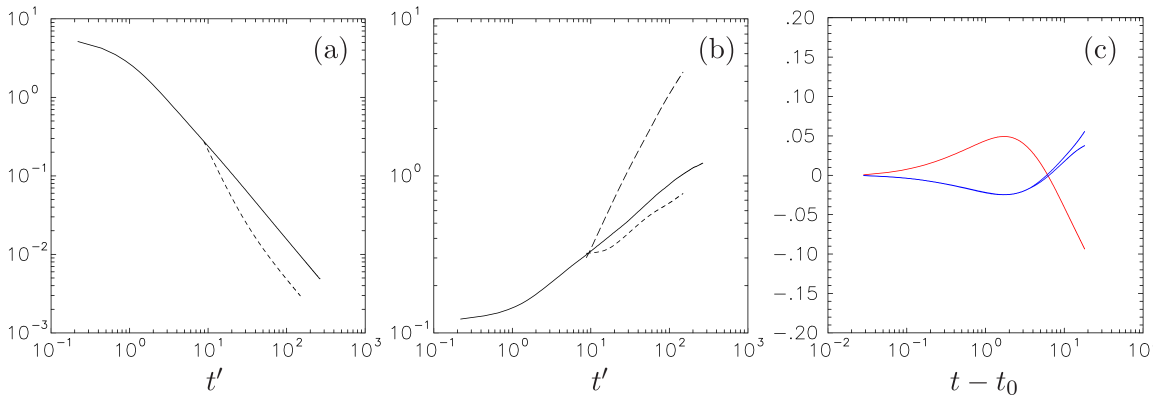

FIG. 2. (a) Turbulence kinetic energy (K), (b) integral length scales L_{11} and L_{22} of velocity components u_1 and u_2, and (c) Reynolds stress anisotropy tensor elements (b_{11} (red), b_{22} and b_{33} (blue)) in 8192×1024^2 simulation on a $16\pi \times (2\pi)^2$ domain with $N = 1$. Time t is measured from the beginning of the pre-simulation, and the magnetic field is turned on at $t = t_0$. In (a) and (b) solid lines represent the pre-simulation (if extended), while dashed line represents MHD results. In (b) L_{11} L_{22} under the magnetic field are indicated by long and short dashed lines respectively.

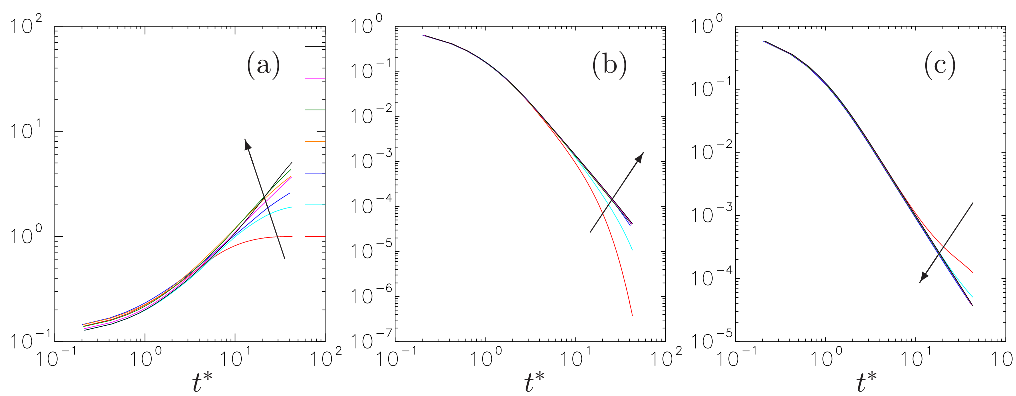

FIG. 3. (a) L_{11}/π, (b) $\langle J\rangle/\langle J\rangle_0$, (c) $\langle\epsilon\rangle/\langle\epsilon\rangle_0$ versus normalized time $t^* = (t - t_0)/(T_E)_0$ since when the magnetic field is turned on. Domain aspect ratio Λ increases from 1 to 64 in the direction of the arrow. Short horizontal bars in (a) mark maximum possible values for each Λ.

may not be apparent if only results at early times were considered.) However, for $\Lambda = 1$ or 2 the growth of L_{11} is clearly constrained by the domain size at later times. It also appears that most results converge (or nearly so) for $\Lambda \geq 8$, at least up to the times shown in the figure.

In Fig. 3 it is worth noting that simulations of low Λ tend to underestimate the Joule dissipation ($\langle J\rangle$) but overestimate the viscous dissipation ($\langle\epsilon\rangle$). This observation can be explained by the forms of the integrands present in the definitions in Eq. (6). The value of $\langle J\rangle$ is determined by a selective sampling of the energy in each Fourier mode, via the factor $(k_x/k)^2$ which is largest for wavevectors pointing in or closely aligned with the k_x direction in wavenumber space. The 3D spectrum $E(\mathbf{k})$ itself takes largest values at low wavenumbers. In a domain of finite length $2\pi\Lambda$ in the x direction the lowest nonzero k_x is $1/\Lambda$. As a result, if Λ is low then some of the Fourier modes that should, via the factor $(k_x/k)^2$, contribute

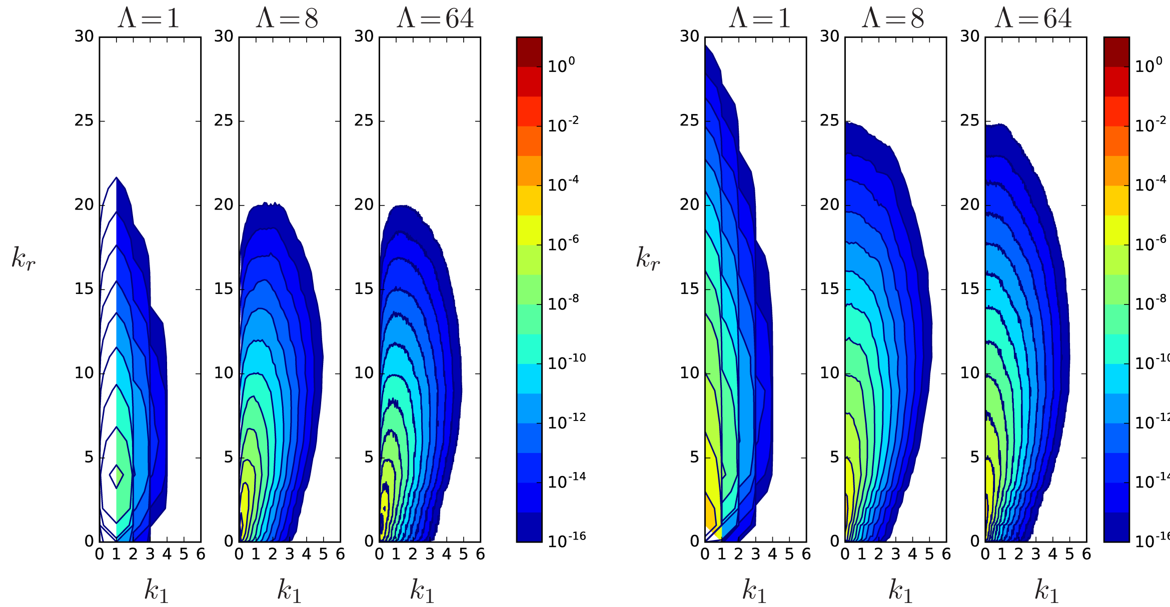

FIG. 4. Contour plots of axisymmetric spectra of Joule dissipation (left frames) and viscous dissipation (right frames), from late-time data in simulations with three different aspect ratios, corresponding to grid resolutions 256^3, 2048×256^2 and 16384×256^2, with $N = 1$ and $(R_\lambda)_0 = 21$.

the most to $\langle J \rangle$ would not have been represented in the simulation.

In Fig 4 we compare the axisymmetric spectra (as functions of k_1 and k_r) in simulations at $\Lambda = 1$, 8 and 64 corresponding to conditions in Fig. 3. In the leftmost frame the space corresponding to $0 < k_x < 1$ is empty because no Fourier modes exist in that range when $\Lambda = 1$. This leads to an underestimate of $\langle J \rangle$ as suggested above. In contrast, for the viscous dissipation, because of the incompressibility condition $\mathbf{u} \perp \mathbf{k}$ in wavenumber space substantial contributions in the range $0 < k_1 < 1$ arise from wavenumber modes of nonzero $k_\perp$. This effect leads to a slight overestimate of $\langle \epsilon \rangle$, although the effect is weak because most of the spectral content of viscous dissipation lies at higher wavenumbers. As in the case of Fig. 3, differences between $\Lambda = 8$ and 64 in Fig. 4 are very small. We conclude that $\Lambda = 8$ is likely to be adequate for minimizing effects of finite domain size in the simulation data presented in this paper.

IV. ANISOTROPY DEVELOPMENT UNDER A MAGNETIC FIELD

Our prime focus of investigation in this paper is the nature of anisotropy development resulting from the magnetic field and its Lorentz force. We consider both quantities sensitive to the large scales and those sensitive to the small scales, followed by a more complete description of scale dependence in spectral space. Most of the results in this section are taken by a simulation with 16384×2048^2 grid points, aspect ratio $\Lambda = 8$, and interaction parameter $N = 1$. Time evolution is expressed in terms of the normalized time t^* which was first used in Fig. 3 (Sec. III). Questions of dependence on N and scaling with respect to Joule time are considered later in Sec. V.

Normal stress parallel to the magnetic field

t^*	b_{11}	$\langle u_1^2\rangle$	$2\langle(p/\rho)s_{11}\rangle$	$\langle J_{11}\rangle$	$\langle\epsilon_{11}\rangle$	relaxation	db_{11}/dt
0.00	-0.00126	0.14800	-8.052×10^{-4}	7.221×10^{-2}	1.334×10^{-1}	-2.537×10^{-1}	0.10600
1.08	0.03424	0.05275	-6.272×10^{-3}	1.756×10^{-2}	2.249×10^{-2}	-4.862×10^{-2}	0.01600
2.06	0.03890	0.02889	-2.656×10^{-3}	7.676×10^{-3}	7.602×10^{-3}	-1.776×10^{-2}	-0.00223
4.87	0.01321	0.01017	-3.842×10^{-4}	1.688×10^{-3}	1.200×10^{-3}	-2.837×10^{-3}	-0.01490
6.86	-0.01141	0.00646	-1.368×10^{-4}	8.525×10^{-4}	5.688×10^{-4}	-1.262×10^{-3}	-0.01480
12.58	-0.07078	0.00269	-4.342×10^{-6}	2.239×10^{-4}	1.517×10^{-4}	-2.779×10^{-4}	-0.00996
26.25	-0.14950	0.00083	5.204×10^{-6}	3.791×10^{-5}	2.845×10^{-5}	-3.994×10^{-5}	-0.00469
41.52	-0.19210	0.00039	2.780×10^{-6}	1.155×10^{-5}	9.121×10^{-6}	-1.168×10^{-5}	-0.00226

Normal stress perpendicular to the magnetic field

t^*	b_{22}	$\langle u_2^2\rangle$	$2\langle(p/\rho)s_{22}\rangle$	$\langle J_{22}\rangle$	$\langle\epsilon_{22}\rangle$	relaxation	db_{22}/dt
0.00	0.00063	0.14890	4.026×10^{-4}	1.460×10^{-1}	1.334×10^{-1}	-2.546×10^{-1}	-0.05330
1.08	-0.01712	0.04538	3.136×10^{-3}	2.727×10^{-2}	1.884×10^{-2}	-4.536×10^{-2}	-0.00800
2.06	-0.01945	0.02436	1.328×10^{-3}	1.056×10^{-2}	5.658×10^{-3}	-1.643×10^{-2}	0.00112
4.87	-0.00661	0.00959	1.921×10^{-4}	1.982×10^{-3}	6.658×10^{-4}	-2.744×10^{-3}	0.00742
6.86	0.00571	0.00680	6.838×10^{-5}	9.752×10^{-4}	2.744×10^{-4}	-1.285×10^{-3}	0.00738
12.58	0.03539	0.00378	2.171×10^{-6}	2.792×10^{-4}	6.230×10^{-5}	-3.342×10^{-4}	0.00498
26.25	0.07475	0.00185	-2.602×10^{-6}	6.269×10^{-5}	1.275×10^{-5}	-6.541×10^{-5}	0.00235
41.52	0.09604	0.00118	-1.390×10^{-6}	2.581×10^{-5}	5.214×10^{-6}	-2.467×10^{-5}	0.00113

TABLE III. Development of terms in the Reynolds stress budget and anisotropy tensor element, from 16384×2048^2 simulation with $\Lambda=8$, $N=1$. The data are listed at several normalized time instants (which are not uniformly spaced).

A. Reynolds stress budget and anisotropy tensor

The Reynolds stress transport equation including the Joule dissipation tensor has already been given in Eq. (4). The corresponding equation for the anisotropy tensor elements is

$$\frac{db_{ij}}{dt}=\frac{1}{2K}\left[2\langle(p/\rho)s_{ij}\rangle-\langle J_{ij}\rangle-\langle\epsilon_{ij}\rangle-\frac{\langle u_iu_j\rangle}{K}\frac{dK}{dt}\right]\ , \qquad (11)$$

where the last term represents a relaxation, or restoring effect. In Table III we show, at selected normalized times t^*, values of the anisotropy tensor elements, mean-squared velocities, various terms in the Reynolds stress equation, and rate of change of anisotropy, in directions parallel and perpendicular to the magnetic field. In the perpendicular direction we have averaged over two coordinate components. At $t^*=0$ the anisotropy is very weak and nonzero only because of sampling errors. However for the Joule dissipation, initially (because of MHD is applied to an isotropic state) $\langle J_{22}\rangle\approx2\langle J_{11}\rangle$. This causes $\langle u_2^2\rangle$ to decrease faster than $\langle u_1^2\rangle$, such that the anisotropy tensor elements b_{11} and b_{22} quickly become positive and negative, respectively. As the turbulence structure adjusts over time, $\langle J_{22}\rangle$ remains stronger than $\langle J_{11}\rangle$ but their difference becomes less dominant. The anisotropizing effect of Joule dissipation is resisted by the behavior of viscous dissipation which is however relatively weak, while the re-distributive pressure-strain correlation is even weaker. It can be seen that at time $t^*\sim1-2$ the relaxation term in Eq. (11) becomes strong enough such that both

db_{11}/dt and db_{22}/dt undergo a change in sign, to be followed by b_{11} and b_{22} themselves at $t^* \approx 6$.

An important question is (e.g. Refs. 22 and 34) whether a strong magnetic field would cause the turbulence to take on a Q2D, or perhaps two-dimensional, three-component (2D-3C) character, where the three velocity components are comparable in magnitude but dependence on one coordinate becomes extremely weak. If strict two-dimensionality occurs then the anisotropy tensor elements would take the values $b_{11} = -1/3$ and $b_{22} = b_{33} = 1/6$. Data at later times in our simulations are qualitatively consistent with development of Q2D behavior. However for a given N the answer to this question requires a study of asymptotic behavior at large times for which domains of extremely large aspect ratios are required to avoid eventual contamination by finite domain-size effects. It is also possible that a higher Reynolds number with a wider range of scales may lead to different outcomes.

B. Small scales and velocity gradient statistics

Since the Lorentz force acts directly at all scale sizes, the small scales are expected to deviate from the classical picture of local isotropy at high Reynolds number. At the same time, because of axisymmetry due to the magnetic field it is useful to distinguish between the statistics of velocity gradients taken in directions parallel or perpendicular to the imposed magnetic field. We introduce the notations $u_{\parallel,\parallel}$, $u_{\parallel,\perp}$, $u_{\perp,\parallel}$, $u^L_{\perp,\perp}$, $u^T_{\perp,\perp}$, where subscripts $\parallel$ and $\perp$ refer to directions along and perpendicular to the magnetic field respectively, and the last two of these refer to longitudinal and transverse velocity gradients in the orthogonal plane. (In our simulations, for example, statistics of $u^T_{\perp,\perp}$ are obtained by taking samples over from $\partial u_2/\partial x_3$ and $\partial u_3/\partial x_2$.) Likewise, for vorticity we distinguish between the statistics of $\omega_\parallel$ and $\omega_\perp$ in the respective directions.

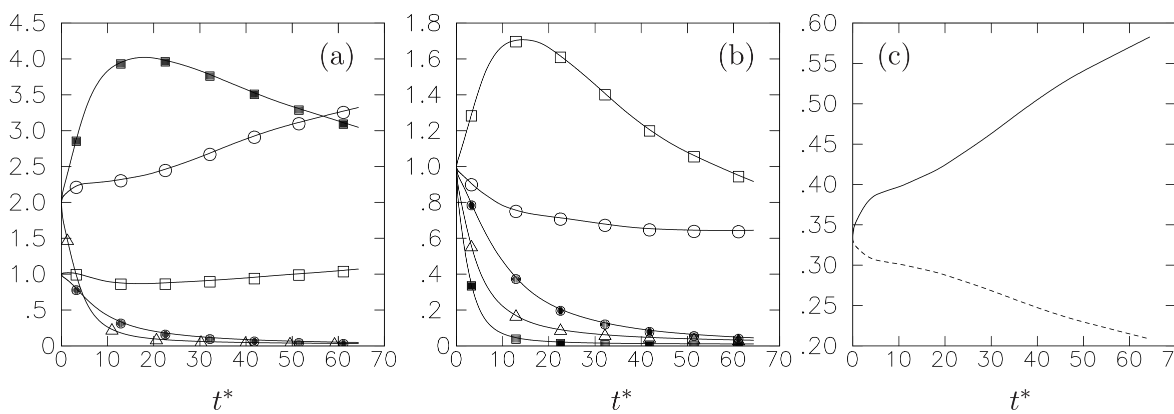

FIG. 5. Development of anisotropy of velocity gradient and vorticity variances, for the same simulation as in Table III. (a) $\langle u^2_{\parallel,\parallel}\rangle$ (●), $\langle u^2_{\parallel,\perp}\rangle$ (■), $\langle u^2_{\perp,\parallel}\rangle$ (△), $\langle (u^L_{\perp,\perp})^2\rangle$ (□), $\langle (u^T_{\perp,\perp})^2\rangle$ (○), all normalized by $\langle\epsilon\rangle/15\nu$; (b) Ratios between variance of velocity gradients: $\langle u^2_{\parallel,\parallel}\rangle/\langle (u^L_{\perp,\perp})^2\rangle$ (●), $\langle u^2_{\perp,\parallel}\rangle/\langle u^2_{\parallel,\perp}\rangle$ (■), for $2\langle u^2_{\parallel,\parallel}\rangle/\langle u^2_{\parallel,\perp}\rangle$ (△), $\langle u^2_{\parallel,\perp}\rangle/\langle (u^T_{\perp,\perp})^2\rangle$ (□), $2\langle (u^L_{\perp,\perp})^2\rangle/\langle (u^T_{\perp,\perp})^2\rangle$ (○); (c) $\langle\omega^2_\parallel\rangle$ (solid lines) and $\langle\omega^2_\perp\rangle$ (dashed lines), both normalized by $\langle\omega_i\omega_i\rangle$.

Figure 5 shows information from the same simulation as in Table III, on (a) the departure of gradient variances from standard isotropy relations, (b) the ratio between variances of different velocity gradients, and (c) the relative contributions from different vorticity components to mean-squared vorticity. In both (a) and (b) it is clear that gradients in the parallel direction become much smaller than those in the perpendicular directions. This implies dependence on x_1 becomes weak compared to x_2 and x_3. The strong decreases seen in $u_{\parallel,\parallel}$ and $u_{\perp,\parallel}$ are accompanied by a strong increase in $u_{\parallel,\perp}$, while the variance of $u_{\perp,\perp}$ shows relatively little change. However at sufficiently large times the transverse gradient in the orthogonal plane, i.e. $u^T_{\perp,\perp}$ ultimately becomes the largest. All of these observations are consistent with a trend towards two-dimensionality in the small scales. In fact for incompressible isotropic turbulence in two dimensions[30,35] the ratio between the mean-squares of transverse to longitudinal velocity gradients is 3.0, which is consistent with the ratio $2\langle(u^L_{\perp,\perp})^2\rangle/\langle(u^T_{\perp,\perp})^2\rangle$ approaching 2/3 closely as seen in frame (b) of this figure. In addition, Q2D behavior in the velocity gradients implies that one vorticity component ($\omega_\parallel$) becomes highly dominant, as seen in frame (c) especially at later times. This observation is consistent with the emergence of elongated vortical structures along the direction of the magnetic field, which can be explained by the principle of conservation of angular momentum[36].

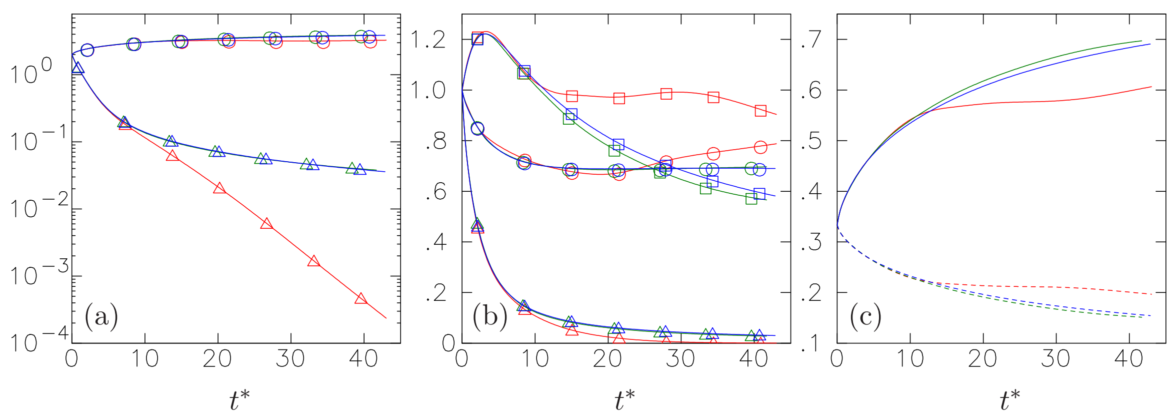

FIG. 6. Development of anisotropy of velocity gradient and vorticity variances under a magnetic field, on domains with aspect ratio $\Lambda = 1$ (red), 8 (green) and 64 (blue) with the shortest dimension having 256 grid points. (a) $\langle u^2_{\perp,\parallel}\rangle$ ($\triangle$), $\langle(u^T_{\perp,\perp})^2\rangle$ ($\circ$), all normalized by $\langle\epsilon\rangle/15\nu$; (b) Ratios between variance of velocity gradients: $2\langle u^2_{\parallel,\parallel}\rangle/\langle u^2_{\parallel,\perp}\rangle$ ($\triangle$), $\langle u^2_{\parallel,\perp}\rangle/\langle(u^T_{\parallel,\perp})^2\rangle$ ($\square$), $2\langle(u^L_{\perp,\perp})^2\rangle/\langle(u^T_{\perp,\perp})^2\rangle$ ($\circ$); (c) $\langle\omega^2_\parallel\rangle$ (solid lines) and $\langle\omega^2_\perp\rangle$ (dashed lines), both normalized by $\langle\omega_i\omega_i\rangle$.

Since velocity gradient statistics are dominated by the small scales, one may ask if they may be not highly sensitive to effects of finite domain size nor forcing applied at the large scales. Indeed, several authors[4,8,22,37] who used cubic domains or simulated forced MHD turbulence have reported results which are qualitatively similar those in Fig. 5. To check for domain size effects in Fig. 6 we compare several results obtained from domains of $\Lambda = 1$, 8, 64 (which were also used for other comparisons in Fig. 3 and 4). Clearly, despite good agreement at early times substantial discrepancies are seen at later times. The differences seen indicate that Q2D character at later times is not as well-defined in the case of $\Lambda = 1$. This is not surprising, since the confining effects of a finite domain size tends to prevent the flow structure to be extended in the parallel direction to greater lengths, thus acting to maintain a degree of dependence of the fluctuating velocity on the x_1 coordinate. Indeed, it is possible that more substantial domain size effects would arise in past simulations in the literature if they were extended to longer times.

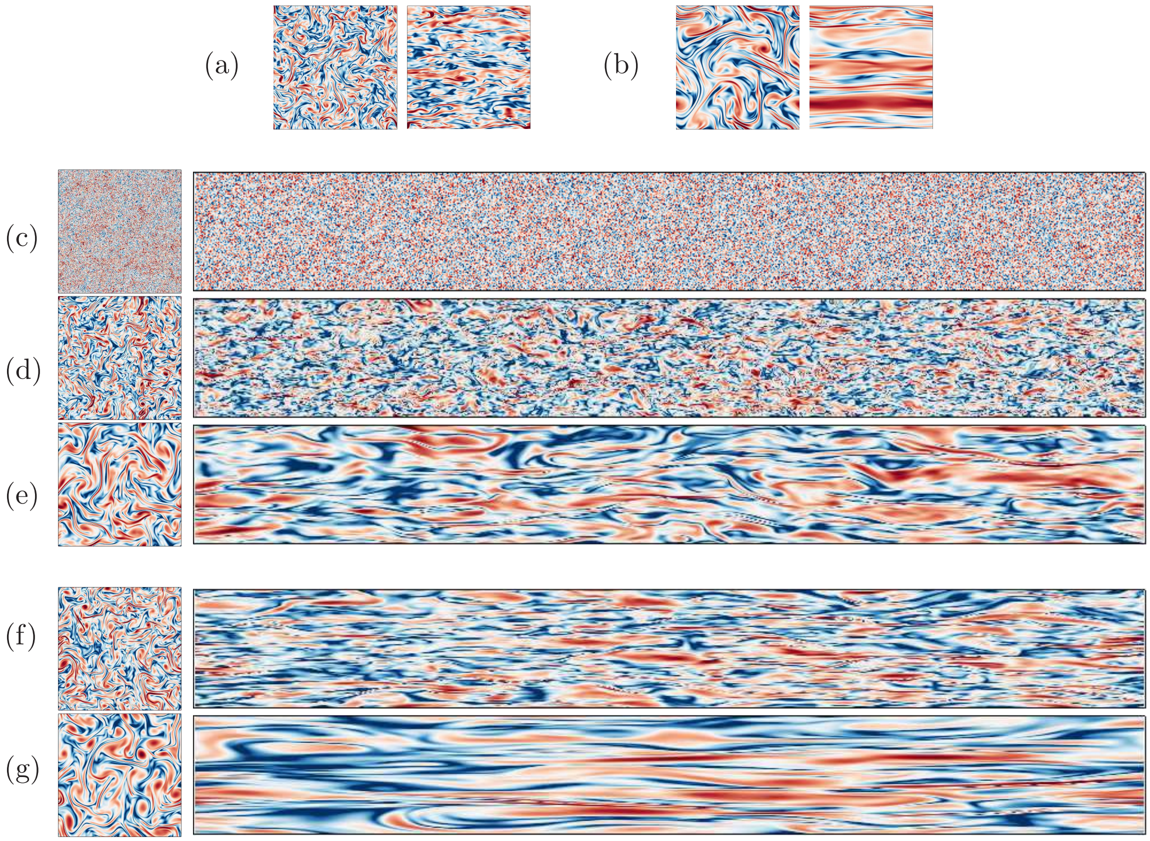

FIG. 7. Visualizations of normalized enstrophy $\Omega/\langle\Omega\rangle$ showing development of coherent vortical structures in MHD turbulence in domains of different aspect ratios. The brighest red and darkest blue represent $\Omega/\langle\Omega\rangle > 10$ and < 0.05 respectively. Each frame is a pair of 2 images in $y-z$ (square, on left) and $x-z$ planes (rectangle, on right.) Frames (a) and (b) are from 2048^3 grid with $\Lambda = 1$, with $N = 1$, at $t^* = 12.58$ and 41.52 respectively; while frames (c), (d), (e) are from 16384×2048^2 grid with $\Lambda = 8$, with $N = 1$, at $t^* = 0$, 12.58 and 41.52. Frames (f) and (g) are similar to (d) and (e), but from simulation at $N = 8$.

As we emphasized earlier in this paper, a long domain in the direction of magnetic field (i.e. one of large aspect ratio) is important in allowing the turbulence structure to evolve naturally. This effect can also be seen by visualization of the enstrophy (Ω, vorticity squared) within two-dimensional cuts taken in planes perpendicular or parallel to the magnetic field. For isotropic turbulence vortical structures are dominated by smaller scales and randomly oriented in space, but we expect them to be stretched out along the direction of the magnetic field. In Fig. 7, comparison of frames (a) and (b) (at two different times) for $\Lambda = 1$ shows that eventually some of the coherent vortical structures become as long as the domain itself (but, due to the nature of periodic boundary conditions, are not allowed to grow any further). This observation is reminiscent of past simulations where later-time results become strongly distorted by the confinement effects of periodic domains of finite size[4,7]. In contrast, frames (c,d,e) show clearly that an elongated domain (with $\Lambda = 8$) along the magnetic field allows the vortex filaments to grow beyond the limit imposed by a domain with $\Lambda = 1$. This contrast shows clearly the benefit of an elongated domain even for supposedly small-scale quantities such as the vorticity. The strong preferential orientation of the observed vortical structures also indicates strong anisotropy. It is also not surprising that this effect is even stronger for larger N, such as in frames (f,g) (for $N = 8$) versus frames (d,e) (for $N = 1$). The effects of large N will be addressed further in Sec. V.

Local axisymmetry for small-scale statistics has some interesting implications for the diagonal elements of the dissipation tensor ($\epsilon_{ij} \equiv 2\nu\langle(\partial u_i/\partial x_k)(\partial u_j/\partial x_k)\rangle$) as well as those of the vorticity covariance tensor ($\langle\omega_i\omega_j\rangle$, whose trace gives the enstrophy, $\langle\Omega\rangle$). In particular, application of relations for locally axisymmetric turbulence derived by George & Hussein[16] leads to the dissipation rates of velocity components parallel and perpendicular to the magnetic field and vorticity component variances being given by

$$\epsilon_\parallel = \langle(u_{\parallel,\parallel})^2\rangle + 2\langle(u_{\parallel,\perp})^2\rangle \ , \tag{12}$$

$$\epsilon_\perp = \langle(u_{\perp,\parallel})^2\rangle + (1/3)\langle(u_{\parallel,\parallel})^2\rangle + (4/3)\langle(u^T_{\perp,\perp})^2\rangle \ , \tag{13}$$

$$\langle\omega_\parallel^2\rangle = -(1/3)\langle u^2_{\parallel,\parallel}\rangle + (8/3)\langle(u^T_{\perp,\perp})^2\rangle \ , \tag{14}$$

$$\langle\omega_\perp^2\rangle = \langle u^2_{\parallel,\parallel}\rangle + \langle u^2_{\perp,\parallel}\rangle + \langle(u_{\parallel,\perp})^2\rangle \ . \tag{15}$$

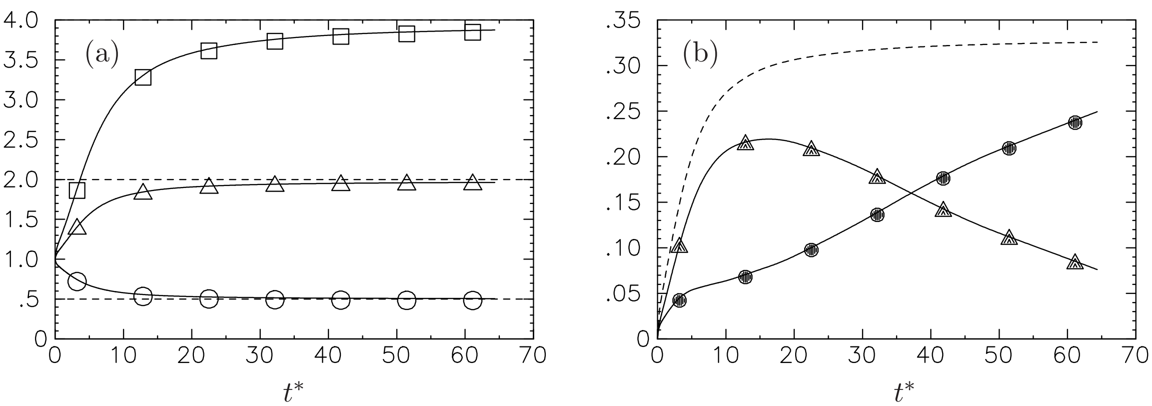

FIG. 8. (a) Evolution of $\epsilon_\parallel/\langle\omega_\perp^2\rangle$ ($\triangle$), $\epsilon_\perp/\langle\omega_\parallel^2\rangle$ ($\bigcirc$) and $(\epsilon_\parallel/\epsilon_\perp)(\langle\omega_\parallel^2\rangle/\langle\omega_\perp^2\rangle)$ ($\square$). Horizontal dashed lines are at values 0.5 and 2.0. (b) Anisotropy tensor elements $d_\parallel = \epsilon_\parallel/(2\epsilon) - 1/3$ for dissipation ($\blacktriangle$), $v_\parallel = \langle\Omega_\parallel\rangle/\langle\Omega\rangle - 1/3$ for vorticity covariance ($\bullet$), and their sum $d_\parallel + v_\parallel$ (dashed line).

Since in MHD turbulence velocity gradients along the parallel direction are strongly suppressed, the relations above can be simplified by keeping the respective last terms which involve gradients in the perpendicular direction. We then obtain

$$\epsilon_\parallel/\langle\Omega_\perp\rangle \approx 2 \ , \quad \epsilon_\perp/\langle\Omega_\parallel\rangle \approx 1/2 \tag{16}$$

(where, for brevity, we denote $\omega_\parallel^2$ and $\omega_\perp^2$ by $\Omega_\parallel$ and $\Omega_\perp$ with $\Omega = \Omega_\parallel + 2\Omega_\perp$) and hence

$$(\epsilon_\parallel/\epsilon_\perp)(\langle\Omega_\parallel\rangle/\langle\Omega_\perp\rangle) \approx 4 \ . \tag{17}$$

Equation (17) gives a relationship between elements of the anisotropy tensors for dissipation and vorticity covariance satisfying local axisymmetry: namely with $d_\parallel = \epsilon_\parallel/(2\epsilon) - 1/3$ and $v_\parallel = \langle\Omega_\parallel\rangle/\langle\Omega\rangle - 1/3$, if $\langle\Omega_\parallel\rangle/\langle\Omega_\perp\rangle = 4/(\epsilon_\parallel/\epsilon_\perp)$ an algebraic rearrangement leads to

$$d_\parallel + v_\parallel = 1/3 \ . \tag{18}$$

t^*	$u_{\parallel,\parallel}$	$u^L_{\perp,\perp}$	$u_{\parallel,\parallel}$	$u^L_{\perp,\perp}$	$u_{\parallel,\perp}$	$u_{\perp,\parallel}$	$u^T_{\perp,\perp}$
	μ_3	μ_3	μ_4	μ_4	μ_4	μ_4	μ_4
0	-0.5290	-0.5286	5.230	5.227	7.345	7.343	7.348
1.08	-0.4611	-0.5507	4.941	4.963	6.593	6.928	6.836
2.06	-0.4173	-0.5605	4.929	4.925	6.427	6.936	6.710
4.87	-0.3309	-0.5299	5.183	4.708	6.333	7.269	6.274
6.86	-0.2783	-0.4844	5.463	4.490	6.452	7.404	5.919
12.58	-0.2138	-0.3443	5.994	3.950	6.894	6.499	5.237
26.25	-0.1023	-0.1643	5.429	3.419	6.940	4.830	4.444
41.52	-0.0211	-0.0901	4.894	3.179	6.480	4.438	4.115
61.44	0.0839	-0.0556	5.553	3.320	6.341	4.222	3.822

TABLE IV. Skewness (μ_3) and flatness (μ_4) factors of the velocity gradients, classified according to statistical axisymmetry as referenced earlier in Sec. IV.B.

Figure 8 shows comparisons of DNS data with (a) Eqs.(16)-(17) and (b) anisotropy tensor elements for the dissipation and vorticity covariance with Eq. (18). Both frames of this figure indicate very good agreement with the asymptotic results at large times.

In addition to second moments, third and fourth moments of the velocity gradients provide important information on nonlinear processes contributing to spectral transfer and intermittency. In 3D isotropic turbulence the longitudinal velocity gradient has a negative skewness of order -0.5 while the transverse velocity gradients have a higher flatness factor (that increases with the Reynolds number). Table IV shows the skewnesses of $u_{\parallel,\parallel}$ and $u^L_{\perp,\perp}$ as well as the flatness factors of all five independent components of the velocity gradients under conditions of axisymmetry. It can be seen that the skewnesses are much reduced, which is consistent with the absence of a forward energy cascade in 2D turbulence. The flatnesses of gradients of $u_\parallel$ show no drastic change but those of the gradients of $u_\perp$ are strongly reduced. This apparent reduction of intermittency in the plane perpendicular to the magnetic field is also consistent with the general absence of intermittency (at least at high Reynolds numbers) in 2D turbulence[38,39].

C. Anisotropy in spectral space

Results in the two preceding subsections indicate both the large scales and the small scales deviate (differently) from isotropy in response to the magnetic field. To characterize anisotropy as a function of scale size it is natural to use a spectral (wavenumber) space description. However, since the observed anisotropy is strong, both magnitude and orientation in wavenumber space should be considered. Information on orientation can be expressed by using the angle between the wavevector $\mathbf{k}$ and the k_1 axis, or by using both k_1 and k_r simultaneously. In practice, the first approach tends to give noisy results at low wavenumbers, since Fourier modes on a Cartesian grid are not uniformly distributed with respect to this nor other angles. We have found simultaneous use of k_1 and k_r to be more convenient. We examine how one-dimensional (1D) spectra (which depend on k_1 and k_r separately) and the axisymmetric energy spectrum (which depend on k_1 and k_r jointly) evolve, as the cumulative result of various physical processes represented in the spectral budget equations.

In isotropic turbulence 1D spectra can be classified as longitudinal and transverse, which

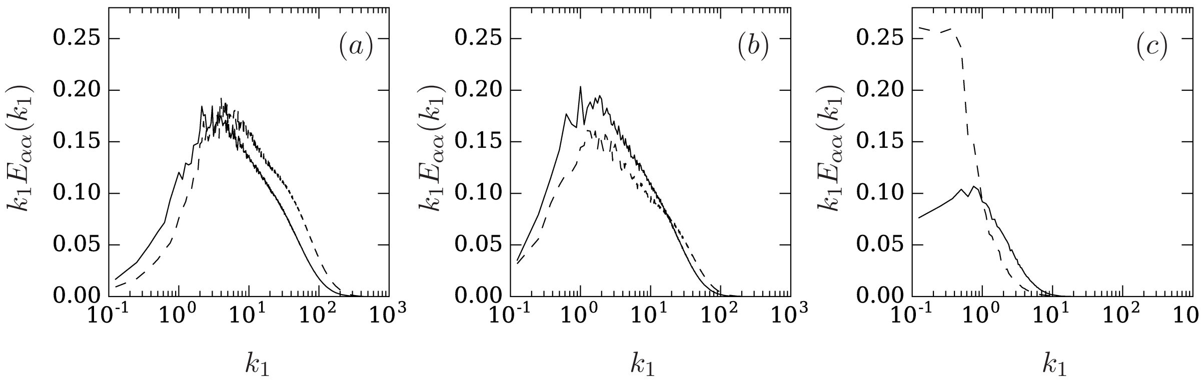

FIG. 9. Compensated 1D spectra $k_1 E_{\alpha\alpha}(k_1)$: solid and dashed lines for $\alpha = 1$ and $\alpha = 2$ respectively. From (a) to (c): at $t^* = 0$, 2.06, 26.25, normalized by the instantaneous kinetic energy.

are related to each other through a constraint based on incompressibility. The reversal of the Reynolds stress anisotropy noted in Sec. IV.A suggests a qualitative change in how longitudinal and transverse spectra compare with each other, especially at low wavenumbers. Figure 9 shows the 1D spectra of u_1 and u_2, as a function of k_1. The scales chosen in the plot here are such that the integral under the curves (in log-linear scales) is equal to the variance of u_1 or u_2 normalized by $K(t)$. At $t^* = 0$ the areas under the two spectra are nearly equal, as required for isotropic turbulence. Subsequently, both spectra are shifted towards smaller k_1, as energy is increasingly concentrated in motions with a large length scale in the x_1 direction. At $t^* = 2.06$, when $\langle u_1^2 \rangle$ has become larger than $\langle u_2^2 \rangle$ (Table III) the spectrum of u_1 is higher than that of u_2 up to $k_1 = 20$. In contrast, at a later time $t^* = 26.25$ when the anisotropy has reversed, the spectrum $E_{22}(k_1)$ has shifted so strongly to low k_1 that it is at least twice of $E_{11}(k_1)$ for $k_1 < 1$. Since integral length scales are proportional to the ratio of 1D spectrum at zero wavenumber to the mean-squared velocity, the features seen at this later time are consistent with a strong growth of integral length scales in the x_1 direction (for all velocity components). Furthermore, Fourier modes of $k_1 < 1$ are present only because the solution domain employed is longer than 2π in the x_1 direction — thus confirming again the importance of using larger or elongated solution domains in the study of MHD effects.

To understand the evolution of the 1D spectra, we need to compute various terms in the spectral evolution equations. For each Fourier mode with wavevector $\mathbf{k}$, the energy spectrum tensor $E_{ij}(\mathbf{k}) \equiv \frac{1}{2}\langle \hat{u}_i^*(\mathbf{k})\hat{u}_j(\mathbf{k}) + \hat{u}_j^*(\mathbf{k})\hat{u}_i(\mathbf{k})\rangle$ (where asterisks for Fourier coefficients denote complex conjugates) evolves by

$$dE_{ij}(\mathbf{k})/dt = -D_{ij}^V(\mathbf{k}) - D_{ij}^J(\mathbf{k}) + \Pi_{ij}(\mathbf{k}) + T_{ij}(\mathbf{k}) \quad (19)$$

where terms on the r.h.s. defined by

$$D_{ij}^V(\mathbf{k}) = 2\nu k^2 E_{ij}(\mathbf{k}) \quad (20)$$

$$D_{ij}^J(\mathbf{k}) = 2(\sigma B_0^2/\rho)\,(k_1/k)^2\, E_{ij}(\mathbf{k}) \quad (21)$$

$$\Pi_{ij}(\mathbf{k}) = ik_i\langle \hat{u}_j^*(\mathbf{k})\hat{p}(\mathbf{k})\rangle - ik_j\langle \hat{u}_i^*(\mathbf{k})\hat{p}(\mathbf{k})\rangle \quad (22)$$

$$T_{ij}(\mathbf{k}) = -\left[\langle ik_m \hat{u}_i^*(\mathbf{k})\widehat{u_j u_m}\rangle + \langle ik_m \hat{u}_j^*(\mathbf{k})\widehat{u_i u_m}\rangle\right] \quad (23)$$

represent viscous dissipation, Joule dissipation, redistribution due to pressure fluctuations and nonlinear spectral transfer respectively. For each term, a 1D spectrum can be formed by summing up contributions in the $k_2 - k_3$ plane at fixed k_1, while an axisymmetric spectrum can be formed by summing over annular rings within this plane.

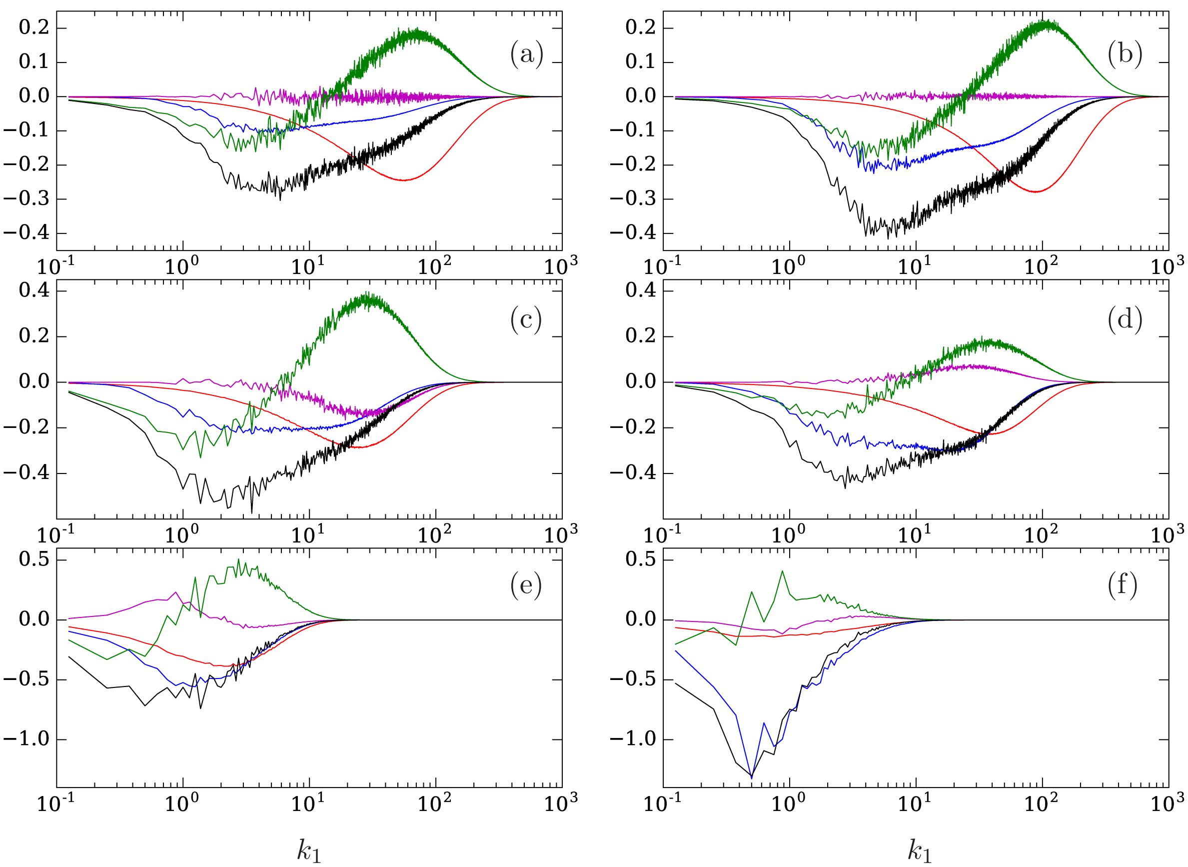

FIG. 10. Terms contributing to the evolution of 1D compensated spectra: (a), (c) and (e) for $d\big(k_1 E_{11}(k_1)\big)/dt$, (b), (d) and (f) for $d\big(k_1 E_{22}(k_1)\big)/dt$, at normalized times (from top to bottom) $t^* = 0$, 2.06, 26.25. Different curves denote time rate of change (black), viscous dissipation (red), Joule dissipation (blue), non-linear transfer (green) and pressure strain correlation (magenta). All are normalized by the instantaneous viscous dissipation.

Figure 10 shows the budget of terms in Eq. (19) for the 1D spectra $E_{11}(k_1)$ (in frames (a,c,e)) and $E_{22}(k_1)$ (in frames (b,d,f)). In general the calculation of spectral quantities at low wavenumber can be affected by errors associated with the number of Fourier modes in a designated wavenumber interval being relatively small. For each given k_1 this effect is more significant if the 1D spectrum concerned is dominated by modes with small k_r. A slight degree of jaggedness is indeed apparent in all curves except for the viscous dissipation, which is dominated by modes of relatively large k_r. At $t^* = 0$ the rates of change of $E_{11}(k_1)$ and $E_{22}(k_2)$ differ mainly as a result of differences between $D^J_{11}(k_1)$ and $D^J_{22}(k_1)$, consistent with the relation $\langle J_{22} \rangle \approx 2\langle J_{11} \rangle$ as discussed in Sec. IV.A. The resulting difference between the rates of change of the two 1D spectra is such that $E_{22}(k_1)$ starts to fall more rapidly than $E_{11}(k_1)$ over a broad wavenumber range, leading to a degree of anisotropy that depends on scale size in the direction of the magnetic field.

It can be seen from frames (c) and (d) above that at $t^* = 2.06$ spectral transfer (green lines) of u_2 from low to high k_1 is significantly weaker than that of u_1. Reduced transfer of u_2 from low k_1 to high k_1 has the effect of slowing down the rate of decrease of $E_{22}(k_1)$ in time. Since this trend is opposite to that observed at $t^* = 0$, this contributes to a gradual weakening, and eventually reversal of anisotropy at later times. At $t^* = 26.25$ all the spectral activity has moved to considerably lower wavenumbers, while the Joule dissipation becomes highly dominant. Finally we note that while pressure-strain correlation term (lines in magenta) is not dominant at any of the three time instants shown, its general effect is to re-distribute energy from the velocity component with more energy to that with less, as reflected in the general change in sign between frames (c,d) and (e,f).

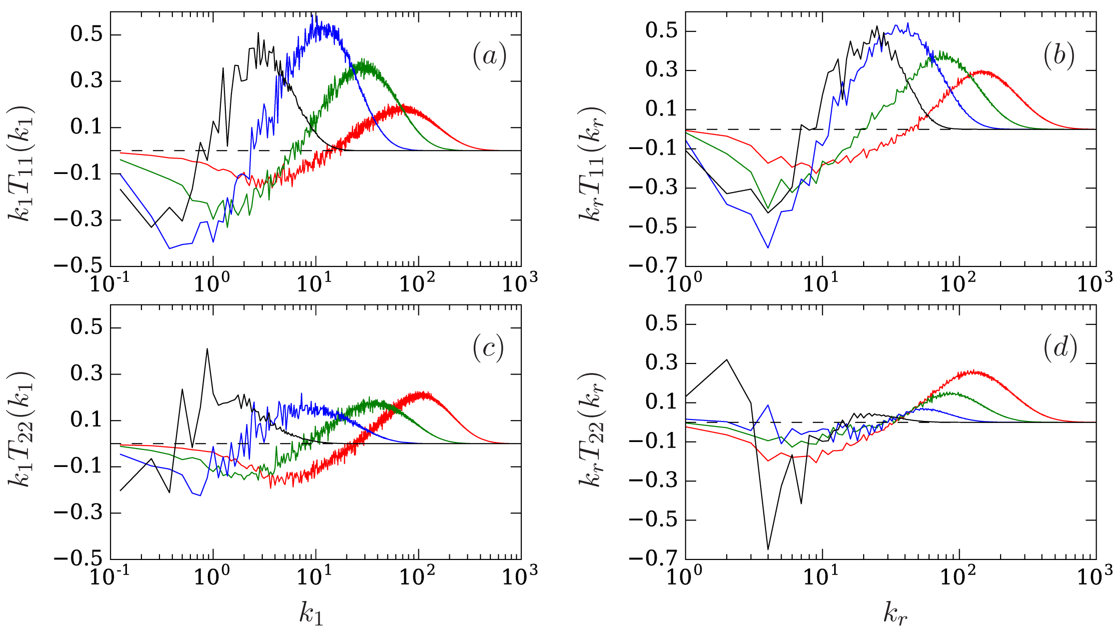

FIG. 11. Evolution of (left) compensated 1D transfer spectra of (a) $k_1T_{11}(k_1)$, (c) $k_1T_{22}(k_1)$, and (right) compensated radial transfer spectra of (b) $k_rT_{11}(k_r)$, (d) $k_rT_{22}(k_r)$. All the spectra shown are normalized by instantaneous viscous dissipation. Lines in red, green, blue and black denote times $t^* = 0$, 2.06, 6.86 and 26.25 respectively.

A more direct illustration of changes in spectral transfer due to the magnetic field is given in Fig. 11, which shows 1D and radial transfer spectra at different times in each frame. In general, as MHD effects cause the turbulence length scales to grow, wavenumber ranges of significant transfer activity are shifted from higher to lower wavenumbers. As this shift to lower wavenumbers continues, energy also becomes increasingly dominated by a small number of Fourier modes, leading to numerical noise which is reflected by the jagged nature of lines in black in this figure. Despite this noise much of the spectral transfer is recognized as being of a "forward cascading" nature, i.e., negative at the lowest few k_1 or k_r values but generally positive for higher wavenumbers. However there is an important exception, in frame (d), where at late times $k_rT_{22}(k_r)$ is positive at the first few values of k_r. This indicates occurrence of backward transfer in the plane perpendicular to the magnetic field. This backward energy transfer in velocity perpendicular to the velocity field has also been reported in forced simulations[40], and is consistent with the transfer characteristics found in two-dimensional three-component turbulence[22,41]. In addition, in this frame, transfer activity at intermediate to higher radial wavenumbers generally becomes weaker in time. This reduction of spectral transfer is consistent with weakened non-Gaussianity for velocity gradients in the orthogonal plane as seen earlier in Table IV.

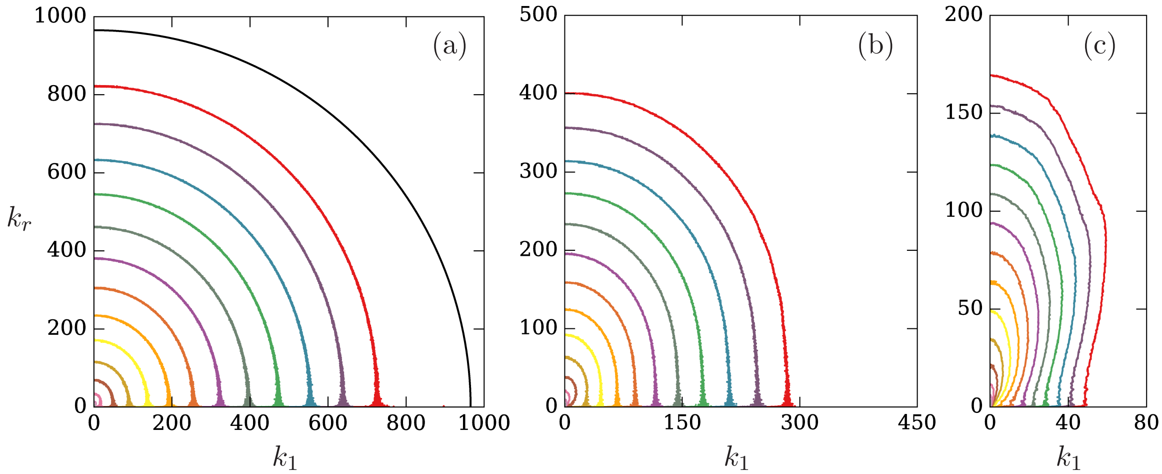

FIG. 12. Contours of axisymmetric energy spectrum $E_A(k_1, k_r)$ at times (from left to right) $t^* = 2.06,\ 6.86,\ 26.25$. Contour levels are set at logarithmically-spaced intervals, decreasing by successive factors of 10 outwards from near the origin. (Note the differences among different frames in the upper limits of the coordinate axes shown. In frame (a) maximum values of both k_1 and k_r are both 960.)

We now turn our attention to axisymmetric spectra, which give more detailed information of energy distribution in Fourier space. Figure 12 shows contour lines of the axisymmetric energy spectrum $E_A(k_1, k_r)$ at three different times (from left to right). As noted in Sec. III, departure from circular contours indicate anisotropy. At $t^* = 2.06$ most contours are at least mildly non-circular: e.g. the curve in red (second counting from outwards) intersects the wavenumber axes at $k_1 \approx 720$ but at $k_r \approx 820$ respectively. To facilitate comparisons in time we have used the same contour levels at different times. However at later times we have had to zoom on lower and lower wavenumbers in order to see all the important features. The contour lines are seen to increasingly deviate from circles. In frame (c) we also observe that the contour lines bend backwards towards smaller k_1 in the region where k_r is also small, showing that energy is increasingly concentrated in Fourier modes with low k_1, i.e. in the plane orthogonal to the magnetic field. These trends are consistent with those seen in forced simulations[40].

Since the magnetic field causes energy to be concentrated at low wavenumbers, we show in Fig. 13 some zoomed-in details for the same spectral region at different times in the simulation. At $t^* = 2.06$ (frame (b)), a departure from isotropy is already evident. At $t^* = 6.86$ (frame (c)) the property of contour lines (at the boundaries between color-coded regions) bending backwards towards $k_1 \approx 0$ at low k_r is well developed. At the last time instant shown (frame (d)) it is clear that energy is increasingly concentrated in a narrow crescent-like region with very small k_1 but a large ratio between k_r and k_1. These results also reaffirm the importance of representing spectral regions of $k_1 < 1$ properly using a domain which is long in the x_1 direction.

To illustrate the effects of different terms in the spectral budget equation on the change of axisymmetric energy spectrum, we show in Fig. 14 the axisymmetric spectrum of each term in Eq. (19). (The pressure-strain correlation term is not shown since it is traceless and does not contribute to changes in the kinetic energy.) To facilitate comparisons between these different terms we have placed frames at a given time horizontally next to each other, and

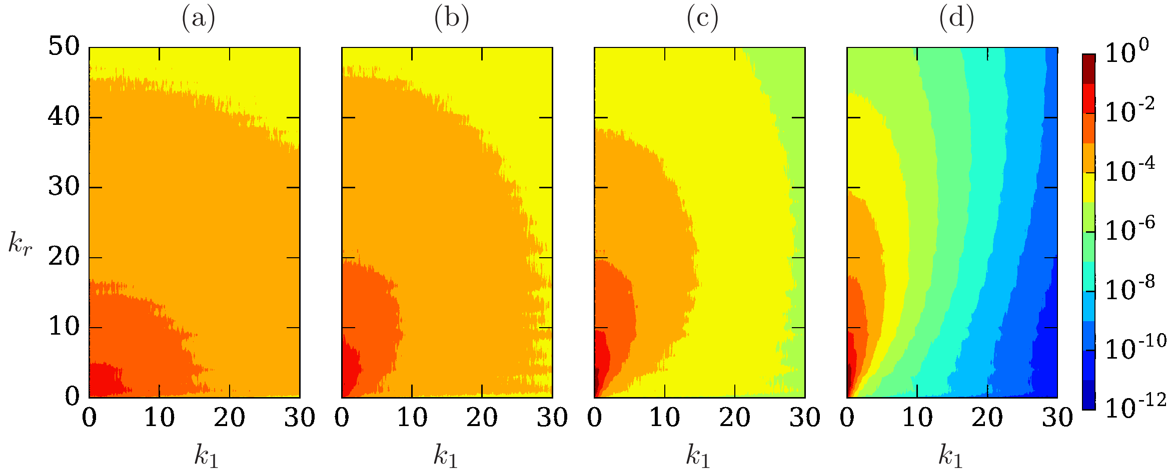

FIG. 13. Axisymmetric spectra of TKE. From left to right, $t^* = 0$, 2.06, 6.86, 26.25.

in contrast to the arrangement in Fig. 13 we now use different upper limits on the k_r axis at different times. In Fig. 14, even at $t^* = 0$ the rate of change (frame (a)) already shows anisotropic character, in which the contours extend to larger k_1 than k_r. This behavior is due to that of the Joule dissipation, which (frame (c)) favors modes of larger k_1 for a given k if the initial velocity field is isotropic. For axisymmetric spectrum of energy transfer, while color contours are used to indicate magnitudes of positive transfers, blank regions indicate negative values — i.e. those modes which are losing energy as a result of the nonlinear interactions. Some degree of noise is present because the transfer is nearly zero in between spectral regions where the spectral transfer is primarily positive or negative respectively. Nevertheless in frame (d) modes losing energy (with negative transfer) can be seen to lie mostly in regions of low k_1 and low k_r, which is consistent with a conventional forward energy cascade.

As time proceeds, down successive rows of Fig. 14, all the axisymmetric spectra undergo substantial changes in both magnitude and shape. A most striking feature is that the spectra for Joule dissipation changes from one that favors modes lying close to the k_1 axis to one that favor modes lying close to the k_r axis. At late times (frame (o)) the Joule dissipation largely resides in a narrow strip next to the k_r axis. The spectrum of viscous dissipation also follows a similar pattern, but later, since it responds to the magnetic field only indirectly via changes in the energy spectrum itself. Zones of negative spectral transfer almost become mostly restricted to the narrow strip near the k_r axis — but it extends to higher values of k_r than seen in zones of highest activity in the other terms. In both frames (l) and (p), at very small k_1, there is a narrow range of k_r where a decrease of k_r leads to a change from negative to positive transfer, which can be taken as a directional form of reverse cascade. Previous studies[3,8,14,42] have also suggested angular transfers from spectral regions with $k_r > k_1$ to $k_r < k_1$. Finally, it may be noted that the contour pattern in frame (m) of this figure (for the rate of change at $t^* = 26.25$) is qualitatively similar to that of the energy itself in frame (d) of Fig. 13. This suggests the shape of the energy spectrum is unlikely to change dramatically if the simulation were to be extended to longer times.

Although viscous dissipation is not the most important term in the discussion above it is worth noting that, as we follow the sequence of frames (b-f-j-n) in Fig. 14 this spectrum increasingly decreases with the wavenumber. In DNS, even in those with forcing, since the

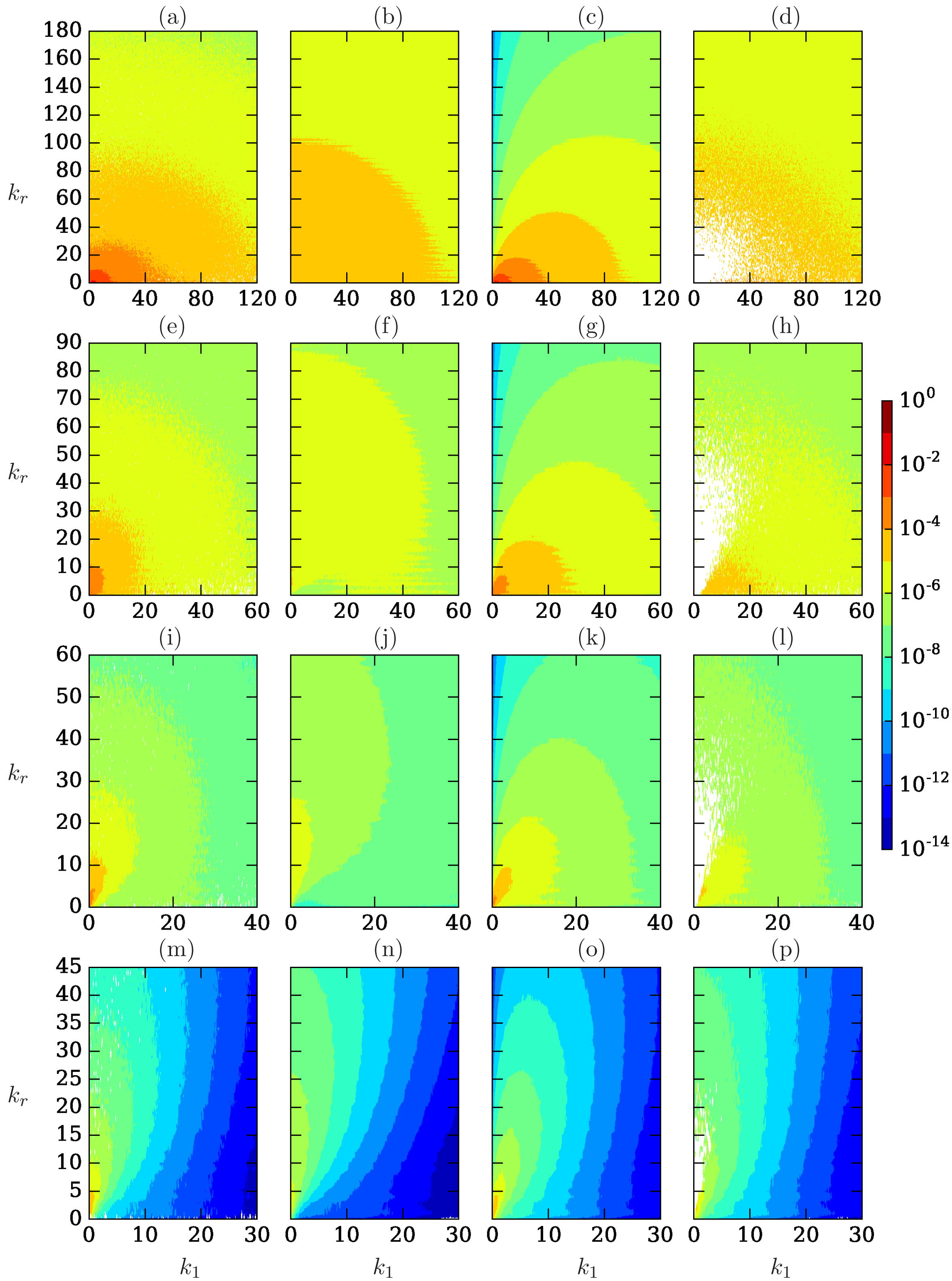

FIG. 14. Axisymmetric spectra of the terms in the energy budget equation. From left to right: (negative of) rate of change, viscous dissipation, Joule dissipation, and positive values of spectral transfer. From top to bottom $t^* = 0$, 2.06, 6.86, 26.25.

range of scales is limited, viscous dissipation spectrum usually peaks at a modest wavenumber. At $t^* = 0$ this peak is well within the pale-orange region in frame (b). Subsequently, since energy and dissipation spectra are related by a kinematic factor of $2\nu k^2$, as the energy spectrum becomes heavily concentrated at the lowest wavenumbers, the same feature occurs in the dissipation spectrum, as well. This explains why in frame (n) we see a strong decrease with increasing wavenumber, especially with respect to k_1 since length scales grow most strongly in this direction.

V. EFFECTS OF THE MAGNETIC INTERACTION PARAMETER

In Sec. IV above we had focused on the case of $N = 1$, i.e. for the ratio of pre-MHD eddy turnover time $T_E = L_{11}/u'$ to Joule time $\tau_J \equiv \rho/(\sigma B_0^2)$ to be equal to unity. If $N > 1$ then the Lorentz force operates at a time scale shorter than the large eddy turnover time, such that the effects of the magnetic field are felt rapidly. As may be expected, a larger N will lead to a more rapid growth of integral length scales, which means numerical requirements in the form of elongated solution domains will become more demanding. Consequently we present data only at modestly large values of N while ensuring numerical results are not grossly contaminated by the effects of finite domain size. In this section we are mainly interested in whether the time evolution of some single-point statistics might scale with the Joule time (which is fixed in time), and how the evolution of some spectral quantities may depend qualitatively on N.

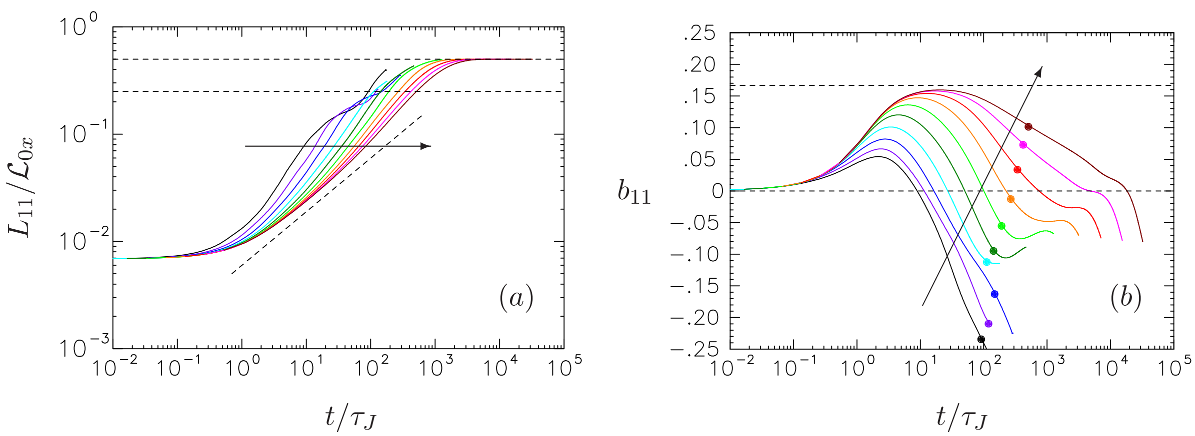

FIG. 15. Evolution of (a) normalized integral length scale and (b) Reynolds stress anisotropy tensor element, in the direction of the magnetic field, with arrows pointing in the direction of increasing N (0.5, 1, 2, 4, 8, ..., 256). In (a), sloping dashed line has slope of 0.5, horizontal dashed lines are at heights 0.25 and 0.5. In (b), solid circles indicate time instants when L_{11} exceeds 1/4 of $\mathcal{L}_{0x}$ as seen in (a). The upper dashed line is at height 1/6.

It is useful to compare results over a series of simulations where the initial turbulence state is the same but N is varied systematically. Per Table II, we have performed such calculations for 10 different values of N, from 0.5 to 256 (in powers of 2), but at a lower grid resolution of 4096×512^2 and a lower pre-MHD Reynolds number. Figure 15 shows the evolution of the integral length scale along the direction of the magnetic field, and the anisotropy tensor element b_{11}, versus time normalized by τ_J. Scaling with Joule time would

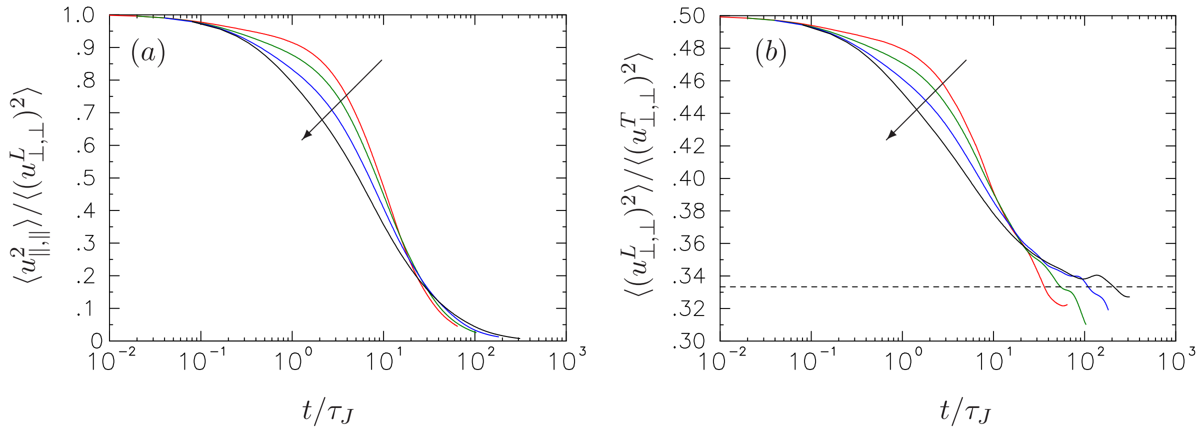

FIG. 16. Evolution of (a) $\langle u^2_{\parallel,\parallel}\rangle/\langle(u^L_{\perp,\perp})^2\rangle$, (b) $\langle(u^L_{\perp,\perp})^2\rangle/\langle(u^T_{\perp,\perp})^2\rangle$. Arrows point in the direction of increasing N $(1, 2, 4, 8)$, for the same 16384×2048^2 domain of $\Lambda = 8$. In (b) the horizontal dashed line denotes 1/3, which is the value in 2D isotropic turbulence.

be indicated if curves for a wide range of N were to coincide. In both frames of this figure this scaling appears to hold better at large N but only at early times up to $t = O(\tau_J)$. In frame (a) a straight line of slope 0.5 on log-log scales is used to compare with a prediction by Okamoto[9] that the ratio $L_{11}/\mathcal{L}_{0x}$ should be proportional to $(t/\tau_J)^{1/2}$ at large N and large t/τ_J. A modest degree of agreement is seen, but results at later times may also be contaminated by domain size effects as L_{11} grows past 1/4 of $\mathcal{L}_{0x}$ and eventually ceases to increase any further upon reaching its maximum possible value of $\mathcal{L}_{0x}/2$. In (b), at large N anisotropy is clearly very strong, with b_{11} almost reaching 1/6, which is the limiting value corresponding to the result $\langle u_1^2\rangle = 2\langle u_2^2\rangle$ predicted by the theory of Moffatt[21] which assumes both viscous and nonlinear transfer effects to be vanishingly small. Another effect of large N is that the integral length scales grow extremely fast, eventually even reaching its maximum value of half of the length of the solution domain. Some of the less well-defined features in the curves for b_{11} at late times (beyond those values of t/τ_J marked by the solid circles on each line) are probably the result of finite domain size effects.

The results in Fig. 15 show how the large scale motions respond to magnetic fields of different strengths (even if the integral scales are still shorter than 1/4 of the domain size). To examine how the small scales respond we next show in Fig. 16 some ratios of the variances of velocity gradients. Since our main interest in the small scales is in departures from local isotropy, we revert back from 4096×512^2 simulations in Fig. 15 to 16384×2048^3 with a higher pre-MHD Reynolds number. In both frames of Fig. 16 the main effect of a larger N is to accelerate, beyond slightly more than 0.1 τ_J, the transition from a state of local isotropy to a new asymptotic state of anisotropy. In frame (a) the ratio between longitudinal gradient variances beyond about 30 τ_J is almost independent of N. In frame (b) the ratio between longitudinal and transverse gradient variances in the orthogonal plane drops to values close to 1/3 (the value for 2D turbulence), although oscillations (presumably arising from finite domain size effects) develop from about 30 τ_J onwards. These results are consistent with a trend towards a Q2D state, whose development is hastened by stronger magnetic fields.

For spectral characteristics, in Fig. 17 we compare the spectral budget for 1D spectra (similar to those in Fig. 10) obtained with $N = 1$ versus $N = 8$. In frames (a) and (c) it is seen that at large N the Joule dissipation dominates the rate of change of the spectrum

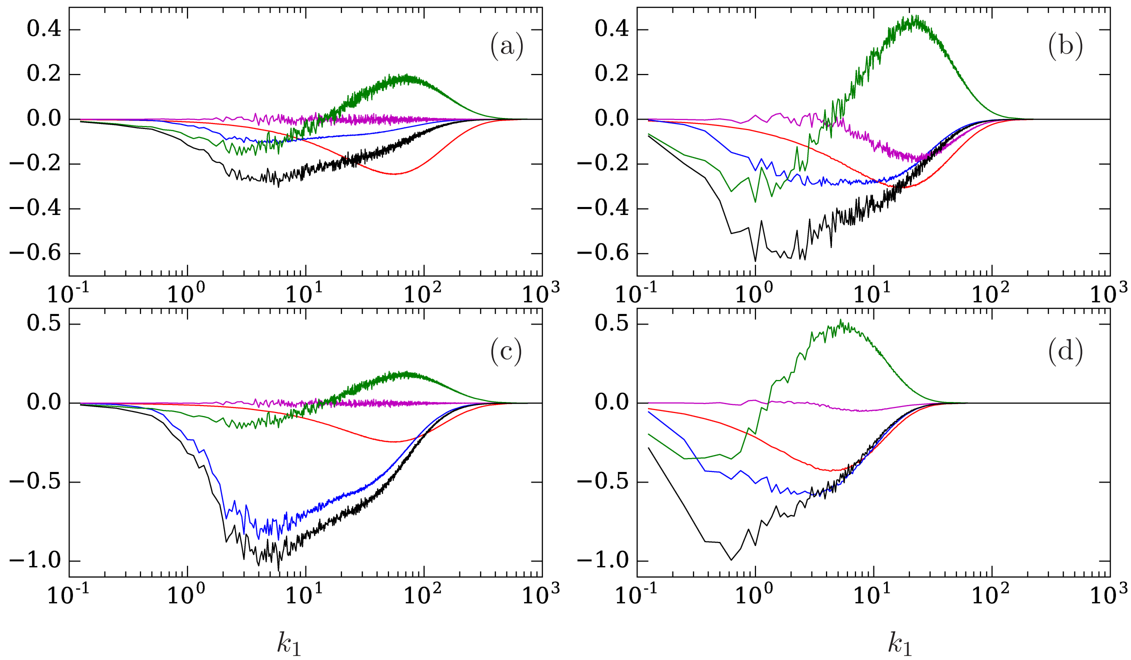

FIG. 17. Terms contributing to the evolution of 1D compensated spectra of: $d\big(k_1 E_{11}(k_1)\big)/dt$: (a) $t^* = 0$, with $N = 1$; (b) $t^* = 3.29$, with $N = 1$; (c) $t^* = 0$, with $N = 8$; (d) $t^* = 3.29$, with $N = 8$. Different curves denote time rate of change (black), viscous dissipation (red), Joule dissipation (blue), non-linear transfer (green) and pressure strain correlation (magenta). All curves are normalized by the instantaneous viscous dissipation.

immediately from $t^* = 0$ onwards. At later times (here $t^* = 3.29$ corresponds to a time close to maximum anisotropy) the bulk of the spectral activity is clearly shifted to lower values of k_1. While both spectral transfer and viscous dissipation become more significant, for k_1 about 8 onwards these two contributions appear to cancel out each other, so that the Joule dissipation still dominates the rate of change overall.

Finally, in Fig. 18 we show axisymmetric spectra of different terms in the spectral energy budget equation, at $N = 8$ in a manner similar to $N = 1$ results in Fig. 14. Frames a-d and e-h of Fig. 18 can be compared with frames a-d and m-p of Fig. 14 respectively, with the same color map being used in both figures. Comparison between frames (a) and (c) shows that at $t^* = 0$ the initial rate of change in regions of strongest activity is dominated by the Joule dissipation, except at very low k_1 and at higher values of k_r. The contours in frame (c) have the same shape as those in frame (c) of fig. 14 but are at higher contour levels and hence shown in a different color. At the later time of $t^* = 26.25$ all four frames in the bottom row are very similar in shape, being concentrated in zones of low k_1 and large k_r. For spectral transfer a narrow crescent-like region of negative values (in white) near the k_r axis persists but is now confined to yet smaller values of k_1.

VI. CONCLUSIONS

In this paper we have presented results from direct numerical simulations of decaying magnetohydrodynamic (MHD) turbulence to study the response of isotropic turbulence to a strong external magnetic field, in the limit of low magnetic Reynolds number (R_m). This

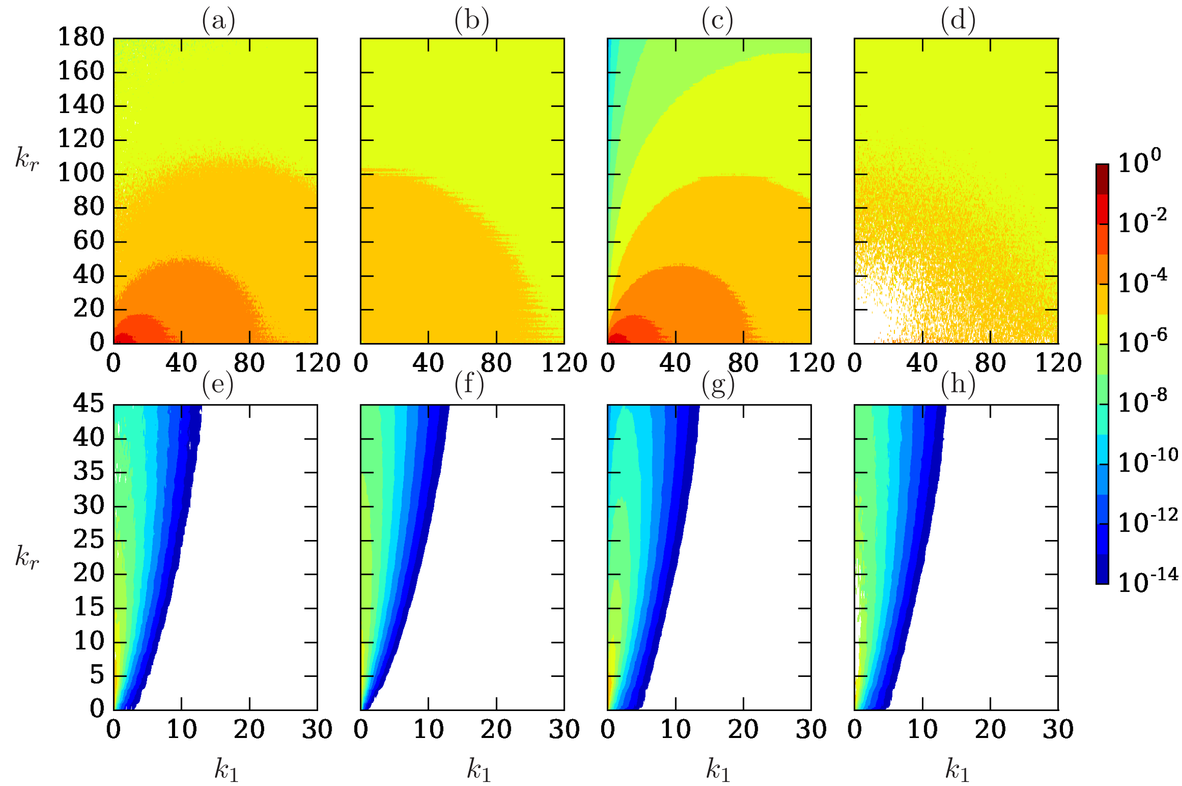

FIG. 18. Axisymmetric spectra of the terms in the energy budget equation at $N = 8$. From left to right: (negative of) rate of change, viscous dissipation, Joule dissipation, and positive values of spectral transfer. Top row for results at $t^* = 0$, bottom row for $t^* = 26.25$.

type of flow, to which a quasi-static approximation applies, is applicable to many terrestrial applications including small-scale flow in planetary cores and industrial applications involving liquid metals. Although this subject has been studied by other authors before, preferential growth of large-eddy length scales in the direction of the magnetic field implies that accurate results cannot be readily obtained, especially at later times, unless the solution domain is very long in this direction. We have used elongated solution domains of aspect ratio 8 for most purposes, and in some cases up to 64. The largest number of grid points was 16384×2048^2, which is much higher than in most previous works for this flow. The strength of the magnetic field is quantified by the magnetic interaction parameter (N) which is the ratio of pre-MHD eddy-turnover time to the Joule time of the magnetic field. A pre-simulation is conducted in a manner that minimizes any effects of numerical distortion. To facilitate a natural response to the magnetic field, no forcing is applied.

In low-R_m MHD turbulence the velocity field is modified by the magnetic field via the Lorentz force, which introduces anisotropy at all scales through the Joule dissipation. With the magnetic field in the x_1 direction, a reversal of Reynolds stress anisotropy is observed in which as $\langle u_1^2 \rangle > \langle u_2^2 \rangle$ at early times but $\langle u_1^2 \rangle < \langle u_2^2 \rangle$ later. Analysis of the Reynolds stress budget shows initially the larger Joule dissipation for u_2 leads to $\langle u_1^2 \rangle > \langle u_2^2 \rangle$, whereas relaxation terms are responsible for the reversal. The small scales also become anisotropic although velocity gradient statistics follow constraints based on a state of local axisymmetry. In the direction of the magnetic field velocity gradients become much weaker while the vorticity component is dominant. The property of local axisymmetry leads to some interesting relations between different components of the dissipation and vorticity-variance tensors. Both large and small scales display trends towards quasi two-dimensionality, including great contrast between integral length scales in different directions, a ratio close to 3 between the mean squares of longitudinal and transverse velocity gradients in the plane, and a reduced intermittency typical of 2D turbulence.

We have also studied in detail anisotropy in spectral space, as a function of wavenumbers parallel and perpendicular (k_1 and k_r respectively) to the magnetic field, through the use of 1D and axisymmetric spectra. As expected, the most important contribution in the spectral dynamics comes from the Joule dissipation, which is counteracted by viscous dissipation, nonlinear transfer, and pressure-strain effects. As the turbulence evolves 1D spectra in k_1 become increasingly concentrated in regions of low k_1, especially for the spectra of u_2 at later times. Radial spectra for u_2 in k_r show signs of a backward transfer in regions of small k_r. Axisymmetric spectra as a function of k_1 and k_r simultaneously show that turbulence kinetic energy is increasingly concentrated in a narrow crescent-like region with very small k_1 but $k_r \gg k_1$. The crescent-like shape results from the anisotropic axisymmetric spectra of Joule dissipation which tends to selectively remove energy from modes in spectral regions where $k_1 > k_r$.

While most of the effort in this paper has been focused on simulations with $N = 1$, we have included results at larger N, which leads to a stronger Joule dissipation and faster growth of length scales in the direction of the magnetic field. Simulations conducted with the same initial turbulence state but N varied over two orders of magnitude indicate that the development of Reynolds stress anisotropy scales with Joule time for about 1 τ_J, and peak anisotropy approaches values predicted at infinitely large N (before a reversal occurs). Other effects of large N include accelerated development of local axisymmetry for statistics of the velocity gradients, and increased dominance of Joule dissipation in the spectral dynamics.

In summary, we wish to emphasize that although previous works on the subject of this paper have been useful, numerical constraints arising from the physics of the effects of a magnetic field must be given careful consideration. In general, our present results on elongated domains confirm those seen in prior work on cubic domains of finite size up to a certain time span, but also provide new information at later times where results on cubic domains could be overwhelmed by numerical confinement effects. For example, from Fig. 3 one may infer that although results from simulations on cubic domains and on elongated domains may be largely in agreement as far as early or even intermediate times are concerned, the benefits of elonagated domains are very substantial if long-time behaviors are to be established with confidence. Figure 7 also shows quite clearly that the development of vortical structures under the magnetic field cannot be represented quite faithfully unless the domain is sufficiently long, the contrasts being increasingly dramatic at later times. Several of the key results in this paper, including relations between contributions to dissipation and enstrophy from derivatives in different directions (Eq. 18), and the behavior of axisymmetric spectra at low wavenumbers (Fig. 14) of various terms in the spectrum tensor equation can be captured accurately only on elongated domains at long simulation times.

In this work, while the bulk of the computing power have been devoted to the use of elongated dimains, the Reynolds numbers for the (unforced) isotropic turbulence states to which the magnetic field is applied have been modest. An important future goal is thus to simulate MHD effects acting on initially isotropic turbulence with an inertial range, which will require yet-larger simulations of greater computational cost. In addition, other fundamental questions include how turbulent mixing is affected by the magnetic field, and how an initially anisotropic turbulent flow may respond. The first of these questions is related to studies of turbulent mixing at Schmidt number much lower than unity[43] which is typical for liquid metals. The second can be coupled to the study of changes in turbulence structure of fluids passed through axisymmetric contraction or other changes of cross-section[18]. Results from simulations designed to address these questions will be reported separately.

ACKNOWLEDGMENTS

The authors gratefully acknowledge support from the Fluid Dynamics Program of the National Science Foundation, under Grant CBET-1510749. The computations and data analyses reported in this paper were performed primarily using advanced computational facilities provided by the Texas Advanced Computation Center (TACC) under the XSEDE program supported by NSF. We thank Professors Peter A. Davidson, Jörg Schumacher and Mahendra K. Verma for helpful discussions. We also thank the reviewers for their valuable comments which have helped us improve the paper.

---

* pk.yeung@ae.gatech.edu.

1 P. A. Davidson, *Turbulence in Rotating, Stratified and Electrically Conducting Fluids* (Cambridge University Press, 2013).
2 D. Biskamp, *Magnetohydrodynamic Turbulence* (Cambridge University Press, 2003).
3 B. Knaepen and R. Moreau, "Magnetohydrodynamic turbulence at low magnetic Reynolds number," Annu. Rev. Fluid Mech. **40**, 23–45 (2008).
4 O. Zikanov and A. Thess, "Direct numerical simulation of forced MHD turbulence at low magnetic Reynolds number," J. Fluid Mech. **358**, 299–333 (1998).
5 T. Ishida and Y. Kaneda, "Small-scale anisotropy in magnetohydrodynamic turbulence under a strong uniform magnetic field," Phys. Fluids **19**, 075104 (2007).
6 P. Burattini, M. Kinet, D. Carati, and B. Knaepen, "Anisotropy of velocity spectra in quasistatic magnetohydrodynamic turbulence," Phys. Fluids **20**, 065110 (2008).
7 K. S. Reddy and M. K. Verma, "Strong anisotropy in quasi-static magnetohydrodynamic turbulence for high interaction parameters," Phys. Fluids **26**, 025109 (2014).
8 U. Schumann, "Numerical simulation of the transition from three-to two-dimensional turbulence under a uniform magnetic field," J. Fluid Mech. **74**, 31–58 (1976).
9 N. Okamoto, P. A. Davidson, and Y. Kaneda, "On the decay of low-magnetic-Reynolds-number in an imposed magnetic field," J. Fluid Mech. **651**, 295–318 (2010).
10 B. Favier, F. S. Godeferd, C. Cambon, and A. Delache, "On the two-dimensionalization of quasistatic magnetohydrodynamic turbulence," Phys. Fluids **22**, 075104 (2010).
11 V. Eswaran and S. B. Pope, "An examination of forcing in direct numerical simulations of turbulence," Comput. Fluids **16**, 257–278 (1988).
12 Y. Kaneda, T. Ishihara, M. Yokokawa, K. Itakura, and A. Uno, "Energy dissipation rate and energy spectrum in high resolution direct numerical simulations of turbulence in a periodic box," Phys. Fluids **15**, L21–L24 (2003).
13 P. K. Yeung, D. A. Donzis, and K. R. Sreenivasan, "Dissipation, enstrophy and pressure statistics in turbulence simulations at high Reynolds numbers," J. Fluid Mech. **700**, 5–15 (2012).

[14] A. Alemany, R. Moreau, P. Sulem, and U. Frisch, "Influence of an external magnetic field on homogeneous MHD turbulence," J. de Mecanique **28**, 277–313 (1979).
[15] J. Sommeria and R. Moreau, "Why, how, and when, MHD turbulence becomes two-dimensional," J. Fluid Mech. **118**, 507–518 (1982).
[16] W. K. George and H. J. Hussein, "Locally axisymmetric turbulence," J. Fluid Mech. **233**, 1–23 (1991).
[17] M. K. Verma, "Anisotropy in quasi-static magnetohydrodynamic turbulence," Rep. Prog. Phys **80** (2017).
[18] M. P. Clay and P. K. Yeung, "A numerical study of turbulence under temporally evolving axisymmetric contraction and subsequent relaxation," J. Fluid Mech. **805**, 460–493 (2016).
[19] B. Teaca, M. K. Verma, B. Knaepen, and D. Carati, "Energy transfers in anisotropic magnetohydrodynamic turbulence," Phys. Rev. E **79**, 046312 (2009).
[20] N. Okamoto, K. Yoshimatsu, K. Schneider, and M. Farge, "Small-scale anisotropic intermittency in magnetohydrodynamic turbulence at low magnetic Reynolds numbers," Phys. Rev. E. **89**, 033013 (2014).
[21] H. K. Moffatt, "On the suppression of turbulence by a uniform magnetic field," J. Fluid Mech. **28**, 571–592 (1967).
[22] B. Favier, F. S. Godeferd, C. Cambon, A. Delache, and W. J. T. Bos, "Quasi-static magnetohydrodynamic turbulence at high Reynolds number," J. Fluid Mech. **681**, 434–461 (2011).
[23] A. Pothérat and K. Kornet, "The decay of wall-bounded MHD turbulence at low R_m," J. Fluid Mech. **783**, 605–636 (2015).
[24] V. Bandaru, T. Boeck, D. Krasnov, and J. Schumacher, "A hybrid finite difference–boundary element procedure for the simulation of turbulent MHD duct flow at finite magnetic Reynolds number," J. Comput. Phys. **304**, 320–339 (2016).
[25] H. Kobayashi, "Large eddy simulation of magnetohydrodynamic turbulent channel flows with local subgrid-scale model based on coherent structures," Phys. Fluids **18**, 045107 (2006).
[26] P. A. Davidson, *An Introduction to Magnetohydrodynamics* (Cambridge University Press, 2001).
[27] R. S. Rogallo, "Numerical experiments in homogeneous turbulence. *NASA Tech. Memo. 81315*, NASA Ames Research Center," (1981).
[28] G. K. Batchelor, "The theory of axisymmetric turbulence," Proc. Roy. Soc. Lond. A **186**, 480–502 (1946).
[29] P. D. Mininni, D. Rosenberg, and A. Pouquet, "Isotropization at small scales of rotating helically driven turbulence," J. Fluid Mech. **699**, 263–279 (2012).
[30] S. B. Pope, *Turbulent Flows* (Cambridge University Press, 2000).
[31] P. K. Yeung and Y. Zhou, "Universality of the Kolmogorov constant in numerical simulations of turbulence," Phys. Rev. E **56**, 1746–1752 (1997).
[32] P. K. Yeung, S. B. Pope, and B. L. Sawford, "Reynolds number dependence of Lagrangian statistics in large numerical simulations of isotropic turbulence," J. Turb. **7**, 1–12 (2006).
[33] P. K. Yeung, S. S. Girimaji, and S. B. Pope, "Straining and scalar dissipation on material surfaces in turbulence: implications for flamelets," Comb. & Flame **79**, 340–365 (1989).
[34] B. Gallet and C. R. Doering, "Exact two-dimensionalization of low-magnetic-Reynolds-number flows subject to a strong magnetic field," J. Fluid Mech. **773**, 154–177 (2015).
[35] T. Gotoh, Y. Watanabe, Y. Shiga, T. Nakano, and E. Suzuki, "Statistical properties of four-dimensional turbulence," Phys. Rev. E. **75**, 016310 (2007).
[36] P. A. Davidson, "The role of angular momentum in the magnetic damping of turbulence," J. Fluid Mech. **336**, 123–150 (1997).

[37] A. Vorobev, O. Zikanov, P. A. Davidson, and B. Knaepen, "Anisotropy of magnetohydrodynamic turbulence at low magnetic Reynolds number," Phys. Fluids **17**, 125105 (2005).

[38] G. Boffetta and R. E. Ecke, "Two-dimensional turbulence," Annu. Rev. Fluid Mech. **44**, 427–451 (2012).

[39] L. M. Smith and V. Yakhot, "Finite-size effects in forced two-dimensional turbulence," J. Fluid Mech. **274**, 115–138 (1994).

[40] K. S. Reddy, R. Kumar, and M. K. Verma, "Anisotropic energy transfers in quasi-static magnetohydrodynamic turbulence," Phys. Plasmas **21**, 102310 (2014).

[41] D. Montgomery and L. Turner, "Two-and-a-half-dimensional magnetohydrodynamic turbulence," Phys. Fluids **25**, 345–349 (1982).

[42] P. Caperan and A. Alemany, "Homogeneous low-magnetic-Reynolds-number MHD turbulence-Study of the transition to the quasi-two-dimensional phase and characterization of its anisotropy," Journal de Mecanique Theorique et Appliquee **4**, 175–200 (1985).

[43] P. K. Yeung and K. R. Sreenivasan, "Spectrum of passive scalars of high molecular diffusivity in turbulent mixing," J. Fluid Mech. **716**, R14 (2013).